Impact of horizontal resolution (1/12° to 1/50°) on Gulf Stream separation, penetration, and variability

Eric P. Chassignet
Xiaobiao Xu

Center for Ocean-Atmospheric Prediction Studies (COAPS)
Florida State University

In press
DOI: 10.1175/JPO-D-17-0031.1

May 31, 2017

Corresponding author: echassignet@fsu.edu

Abstract

The impact of horizontal resolution (1/12° to 1/50°; 6 to 1.5 km at mid-latitudes) on Gulf Stream separation, penetration, and variability is quantified in a series of identical North Atlantic experiments. The questions we seek to address are two-fold: (a) Is the realism of the modeled solution increased as resolution is increased? and (b) How robust is the modeled mesoscale and sub-mesoscale eddy activity as a function of grid spacing and how representative is it of interior quasigeostrophic (QG) or surface quasigeostrophic (SQG) turbulence? We show that (a) the representation of Gulf Stream penetration and associated recirculating gyres shifts from unrealistic to realistic when the resolution is increased to 1/50° and when the non-linear effects of the submesoscale eddies intensifies the mid-latitude jet and increases its penetration eastward, (b) the penetration of into the deep ocean drastically increases with resolution and closely resembles the observations, and (c) surface power spectra in the 70-250 km mesoscale range are independent of the horizontal resolution and of the latitude, and are representative of 2D QG and SQG turbulence.

1. Introduction

Convergence studies are unusual because parameters are often changed as resolution is increased. Here, we follow in the footsteps of Hurlburt and Hogan (2000), Smith et al. (2000), Oschlies (2002), Bryan et al. (2007), Levy et al. (2010), Thoppil et al. (2011), Marzocchi et al. (2015), and Biri et al. (2016) by reporting on the impact of horizontal resolution (1/12° to 1/50°) on Gulf Stream separation, penetration, and variability using a series of identical North Atlantic experiments. The questions we seek to address are two-fold: (a) Is the realism of the modeled solution increased as resolution is increased? and (b) How robust is the modeled mesoscale and sub-mesoscale eddy activity as a function of grid spacing and how representative is it of interior quasigeostrophic (QG) or surface quasigeostrophic (SQG) turbulence?

It is generally recognized that a minimum resolution of 1/10° is required for a proper representation of mid-latitudes western boundary currents and associated eddies (Paiva et al., 1999; Smith et al., 2000; Maltrud and McClean, 2005; Chassignet and Marshall, 2008). A grid spacing of 1/10°, however, is not sufficient to resolve the Rossby radius of deformation with two grid points at all latitudes (Hallberg, 2013) and therefore does not allow for a proper representation of baroclinic instability and associated eddies throughout the domain. Furthermore, effective resolution is limited by the numerical dissipation range (Soufflet et al., 2016) and models with resolution on the order of 1/10° are now being referred as eddying models while eddy-resolving models are configurations that truly resolve the first Rossby radius of deformation throughout the domain (CLIVAR Exchanges special issue, 2014). Despite the major improvements observed with 1/10° grid spacing, the solutions remain extremely sensitive to choices in boundary conditions and subgridscale parameterizations (Ezer and Mellor, 2000; Chassignet and Garraffo, 2001; Bryan et al., 2007; Chassignet and Marshall, 2008) and there is a continuous need to quantify the value added of increased resolution. Furthermore, horizontal resolution of the O(1) km is required to explicitly resolve submesoscale motions with an horizontal scale of the O(10) km. Submesoscale physics have been shown to play a significant role in the vertical fluxes of mass, buoyancy, and tracers (Thomas et al., 2008; Capet et al., 2008; Fox-Kemper et al., 2008; Klein et al., 2011; Roullet et al., 2012; Capet et al., 2016). However, only a few studies have been able to report on the impact of the submesoscale motions on the large scale oceanic circulation because of the computing cost associated with numerical simulations with O(1) km grid spacing. Using a hydrodynamic (no active thermodynamics) model, Hurlburt and Hogan (2000) showed a significant improvement in western boundary current pathways with increased resolution (1/16°, 1/32°, and 1/64°, respectively). Levy et al. (2010) compared the mean characteristics of an idealized flat bottom basin-scale seasonally subtropical and subpolar gyres configuration in a suite of numerical experiments varying in horizontal resolution (1°, 1/9°, and 1/54°). They found that the non-linear effects of the submesoscale eddies that emerge at 1/54° strongly intensifies the jet that separates the two gyres, making it more zonal and penetrating further to the east. The authors states that their results are presumably highly constrained by the idealized geometry of their domain, but we find that many of their results carry over to our series of identical North Atlantic experiments (1/12°, 1/25°, and 1/50°, respectively).

In this paper, we show that (a) the representation of Gulf Stream penetration and associated recirculating gyres shifts from unrealistic to realistic when the resolution is increased to 1/50°, (b) the penetration of EKE into the deep ocean is drastically different and closely resembles observations, and (c) surface power spectra in the 70-250 km mesoscale range are independent of the horizontal resolution and of the latitude, and are representative of 2D QG and SQG turbulence (k^{-5} SSH spectra in energetic regions, not as steep in quiescent regions). The paper is organized as follows. Section 2 describes the model configuration and spin-up procedure. The surface mean and turbulent circulation is discussed in section 3 as a function of resolution and in comparison to observations. It also focuses on the impact of ageostrophic motions on the representation of surface eddy kinetic energy and the fact that current altimetry measurements likely underestimates surface eddy kinetic energy by as much as 30%. The impact of resolution on the deep ocean circulation is shown to be quite significant in section 4. Power spectra are used in section 5 to quantify the degree of 2D QG and SQG turbulence present in the numerical simulations. Finally, the results are summarized in section 6.

2. Model configuration and spin-up

The HYbrid Coordinate Ocean Model (HYCOM) configuration used in this paper is identical to that of Xu et al. (2010, 2012, 2014, 2015, 2016) and covers the North Atlantic from 28°S to 80°N (Fig. 1). The vertical coordinate in HYCOM (Bleck, 2002) is isopycnal in the stratified open ocean and makes a dynamically smooth and time dependent transition to terrain-following in shallow coastal regions and to fixed pressure levels in the surface mixed layer and/or unstratified seas (Chassignet et al., 2003; Chassignet et al., 2006). No inflow or outflow is prescribed at the northern and southern boundaries. Within a buffer zone of about 3° from the northern and southern boundaries, the 3-D model temperature, salinity, and depth of isopycnal interface are restored to the monthly Generalized Digital Environmental Model (GDEM) (Teague et al., 1990; Carnes, 2009) climatology with an e-folding time of 5-60 days that increases with distance from the boundary.

The horizontal resolution for the three experiments are 1/12°, 1/25°, and 1/50° (9, 4.5, and 2.25 km at the equator; 6, 3, 1.5 km in the Gulf Stream region, respectively). The 1/12° model topography is based on the 2’ Naval Research Laboratory (NRL) digital bathymetry database, which combines the global topography based on satellite altimetry of Smith and Sandwell (1997) with several high-resolution regional databases ("http: //www7320.nrlssc.navy.mil/DBDB2_WWW" for documentation). The 1/25° and 1/50° topographies are linearly interpolated from the 1/12° topography and do not contain additional high-resolution topographic features. In the vertical, the simulation contains 32 hybrid layers with density referenced to 2000 m (σ_2): 28.10, 28.90, 29.70, 30.50, 30.95, 31.50, 32.05, 32.60, 33.15, 33.70, 34.25, 34.75, 35.15, 35.50, 35.80, 36.04, 36.20, 36.38, 36.52, 36.62, 36.70, 36.77, 36.83, 36.89, 36.97, 37.02, 37.06, 37.09, 37.11, 37.13, 37.15, and 37.20 kg m^{-3}. The 1/12° configuration resolves the first Rossby radius of deformation up to 60°N while the 1/50° resolves it everywhere (Hallberg, 2013). Furthermore, the 1.5 km grid spacing of the 1/50° configuration resolves up to the fifth internal Rossby radii of deformation at mid-latitudes, based on the above density distribution of the hybrid layers. As in Chassignet and Garraffo (2001) and Xu et al. (2010), the horizontal viscosity operator is a combination of Laplacian ($A_2 = \max(0.05\Delta x^2$ x deformation tensor, A) and bihamonic ($A_4 = V_4\Delta x^3$). The viscosity and diffusion parameters are listed in Table 1. The values for the coefficients in the 1/25° decrease as a function of the grid size and are half that of the 1/12°. The values for the coefficients in the 1/50° are kept close to that of the 1/25°, in order to isolate the impact of resolving the submesoscale on the solution. The K-profile parameterization of Large et al. (1994) is used for vertical mixing in the surface mixed layer as well as in the ocean interior. The bottom drag is quadratic with a coefficient of 10^{-3} and a background RMS flow speed of $5\text{x}10^{-2}$ m/s.

Sea-ice related processes are modeled using an “energy loan” where freezing takes place whenever latent heat is needed to keep the mixed layer temperature from dropping below the freezing level. When the ocean-ice system is being heated, the incoming energy is used to melt the ice before the water temperature is allowed to rise above the freezing level (Semtner, 1976).

The three configurations are initialized using potential temperature and salinity from the GDEM climatology and were spun-up from rest for 20 years (Fig. 2) using climatological atmospheric forcing from the ECMWF reanalysis ERA40 (Uppala et al., 2005) with 3-hourly wind anomalies from the Fleet Numerical Meteorology and Oceanography Center 3 hourly Navy Operational Global Atmospheric Prediction System (NOGAPS) for the year 2003. The year 2003 is considered to be a neutral year over the 1993-present time frame in term of long-term atmospheric pattern the North Atlantic Oscillation (NAO). Heat fluxes are computed using the bulk formulae of Kara et al. (2005). The freshwater flux (evaporation, precipitation, and river runoffs) is treated as a virtual salinity flux and the sea surface salinity (SSS) is restored to monthly climatology with a piston velocity of 15 m/30 days. The salinity difference (between model and climatology) in SSS restoring is clipped to be 0.5 psu to diminish the damping effect of the restoring on ocean fronts (see Griffies et al, 2009, for a discussion). There is no tidal forcing.

Figure 2 shows the time evolution of the mean kinetic energy for the three experiments. It takes approximately 5 years for the energy to stabilize which is the time it takes for the first baroclinic mode Rossby wave to cross the Atlantic basin. The 1/25° is 50% more energetic than the 1/12°, not surprising since the viscosity/dissipation was cut in half when the resolution was increased. The 1/50°, on the other hand, has a mean kinetic energy level similar to the 1/25°. This is expected since the viscosity/dissipation was kept close to that of the 1/25° as the resolution was increased. The slight increase in mean kinetic energy is attributed to the increase in mesoscale and submesoscale activity (discussion in section 3.b). Other integrated values such as the Florida Straits transport (30.8, 34.8, and 34.9 Sv, respectively) and the average overturning streamfunction at 26ºN (17.7, 17.8, and 17.5 Sv respectively) are in reasonable agreement with the observed values of ~32 Sv (e.g., Meinen et al., 2010) and ~17Sv (e.g., McCarthy et al., 2015), respectively.

3. Surface fields

a. Mean circulation

The mean SSH and the mean surface kinetic energy over the last 5 years of the three simulations are compared to the mean SSH field derived from observations (Rio et al., 2014) over the Gulf Stream region (30-80°W, 30-55°N) in Figs. 3 and 4, respectively. Traditionally, a proper representation of the Gulf Stream separation in ocean numerical models has been a challenge (see Chassignet and Marshall, 2008, for a review) and still remains an issue for many configurations despite the fact the major improvements are realized when one uses an horizontal resolution on the order of 1/10° (Bryan et al., 2007). In all three simulations, the Gulf Stream separates at the correct location at Cape Hatteras, but its eastward penetration into the interior differs greatly. At 1/12°, the modeled Gulf Stream (Fig. 3e) does not penetrate far into the interior and the recirculating gyre (Fig. 3e) and highest eddy kinetic energy (Figs. 7c, 8c) are confined west of the New England seamounts (60°W), results that have already been reported in Chassignet and Garraffo (2001), Haza et al. (2007), and Chassignet and Marshall (2008). The 1/25° simulation does not show a lot of improvement over the 1/12° simulation. It is arguably worse since the Gulf Stream in the 1/25° simulation not only does not extend as a coherent feature past the New England seamounts (Fig. 4d), it exhibits an unrealistically strong recirculating gyre southeast of Cape Hatteras (Fig. 3d), and has excessive surface variability (Figs. 7d, 8d) west of 60°W. It is only when the resolution is increased to 1/50° (Fig. 3c) that the Gulf Stream system appears to settle in a pattern that resembles the observations (Fig. 3a). The Gulf Stream penetration, recirculation gyre, and extension qualitatively compare very well with the latest AVISO CNES-CLS mean dynamic topography (MDT) (Fig. 3a).

In order to validate the position of the current main axis as well as the width and intensity of the currents, one needs to be able to perform quantitative model-data comparisons on the scales of interest (i.e., tens of kilometers). There is not of lot of in-situ observations that can be directly compared to the model results on those scales, but global climatologies have come a long way by combining altimetry, direct measurements, and surface drifters (see Rio et al., 2014 for a review) and are now able to provide MDT fields with a sharp definition of the western boundary ocean currents and associated fronts. There is however still quite a few uncertainties associated with these climatologies as shown by the differences between the 2009 and the 2013 CNES-CLS 1/4° climatologies (Fig. 3a,b) (Rio et al., 2011, 2014, respectively). Improvements in the 2013 MDT from the 2009 MDT arise mostly from using a geoid based on the GOCE (Gravity and Ocean Circulation Experiment) instead of one based on the previous Gravity Recovery and Climate Experiment (GRACE) mission and from removing previously undetected undrogued drifters from the drifting buoy velocities distributed by the Surface Drifter Data Assembly Center (SD-DAC) (Grodsky et al., 2011).

Comparison of the model results to these climatologies can be supplemented by comparison to mean dynamic topography constructed along altimetric satellite ground tracks using direct in-situ measurements (Carnes et al., 1990; Blaha and Lunde, 1992; Chassignet and Marshall, 2008). Fig. 5a shows the location of bathythermographic data taken during flights under the TOPEX altimeter ground track 93253A in September 1993 (courtesy of the Altimetry Data Fusion Center, Naval Oceanographic Office) where the mean dynamic topography was computed making the assumption that the dynamic topography relative to the geoid can be approximated by the dynamic height relative to a deep pressure surface which is parallel to the geoid (i.e., a level of no motion). Any error in this assumption will lead to different values of mean dynamic topography, but for the spatial scales of interest, as long as the level of no motion is deep enough, choosing a different level just adds or removes a bias. Fig 5b shows the mean SSH along track 93253A from observations (derived from the bathythermographic data, CNES-CLS09, and CNES-CLS13) and from the 3 numerical simulations (1/12°, 1/25°, and 1/50°). The latest CNES-CLS13 climatology is closest to the MDT derived from the bathythermographic data while the CNES-CLS09 profile shows a much stronger southern recirculation, very likely from contamination by the undrogued drifters which are significantly impacted by wind slippage (Rio et al., 2014). As expected, the 1/50° simulation is closest to the observations with an SSH slope very close to the observations. The slope is weaker in both the 1/12° and 1/25° simulations with the 1/25° exhibiting the biggest departure south of 36°N where the model is unrealistically energetic.

The 5-year modeled mean surface velocity can also be compared to the long term 20-year ADCP mean velocity measurements (Fig. 6) made by the Oleander between the U.S. East Coast and Bermuda (Rossby et al., 2014) from 1993 to 2012. As for the mean SSH, the mean position and direction of the 1/50° current vectors is closest to the observations with the 1/25° being too far south and oriented meridionally and the 1/12° being too zonal. The width of the Gulf Stream is however slightly wider in the 1/50° model than in the observations, indicating more fluctuations of the mean axis of the Gulf Stream in the model. The maximum mean speed of the 1/50° modeled Gulf Stream (0.9 m/s) is also a little less than observed (~1 m/s) (Rossby et al., 2010, 2014) .

b. Fluctuations

Figure 7 shows the root mean square (RMS) of the SSH for the AVISO observations and the three numerical simulations. The AVISO observations are based on 20 years of altimetry (1993-2012) and the modeled RMS fields are for the last 5 years of the simulations. As mentioned above in section 3a, both the 1/12° and 1/25° eddy variability are confined west of 60°W and the chain of New England seamounts. The 1/25° simulation also shows excessive variability southwest of the Gulf Stream axis, which is reflected in the mean SSH field. The overall distribution of the RMS SSH in the 1/50° is in reasonable agreement with the observations, especially the zonal extent, but it is significantly larger in magnitude, especially around the New England seamounts. We will argue below that the difference is primarily due to the fact that altimetry only resolves eddies on O(150) km over a 10-day window. The RMS SSH results reported here are consistent with the distribution obtained by Hurlburt and Hogan (2000) using the 6-layer hydrodynamic (no active thermodynamics) NLOM model (Fig. 8). They also found that the eddy variability remained west of the New England seamounts for their 1/16° and 1/32° (equivalent to our 1/12° and 1/25°) and extend south for their 1/32°. It is only at 1/64° (equivalent to our 1/50°) that the variability extends further eastward. This seems to imply that resolving submesoscale features of the O(10) km is a prerequisite for a correct eastward penetration of the Gulf Stream and the establishment of the recirculating gyres.

Figure 9 displays the observed and modeled surface EKE generated using the geostrophic velocities computed from the SSH fields. As for the RMS, the overall distribution of the surface 1/50° EKE is in reasonable agreement with the observations, especially the zonal extent, but it is significantly larger in magnitude. The surface EKE shown in Fig. 9, however, does not take into account ageostrophic motions and this raises the question as to how significant is the ageostrophic EKE component. Presumably, ageostrophic flows should become more significant as the resolution is increased and submesoscale features arise. Fig. 10 displays the difference between the two components. The most striking feature is the asymmetry between the areas north and south of the Gulf Stream main axis, with the ageostrophic contribution being negative (positive) south (north) of the Gulf Stream. This asymmetry can be explained by considering that the largest ageostrophic contribution arises in area where the flow curvature is significant (meanders, eddies) and where the velocities deviate from geostrophy and satisfy the gradient wind balance, i.e., a primary balance between the centripetal acceleration, the Coriolis acceleration, and the horizontal pressure gradient force (Douglass and Richman, 2015). Outside the Gulf Stream and high energetic areas, the surface Ekman flow becomes dominant. Ageostrophic motions are approximately 10 to 20% of the total velocity in energetic areas of the Gulf Stream and can be as high as 200% in areas dominated by the surface Ekman flow (Fig. 11). A zoom on the region defined by the red rectangle in Figure 11 shows that the ageostrophic motion in the eddies is always anticyclonic (Fig. 12). This is because the centrifugal force associated with the flow curvature is not taken into account when using the geostrophic balance, which results in the rotational velocities being under (over) estimated in anticyclones (cyclones) (Chassignet et al., 1990).

The EKE map displayed in Figure 9a was derived from along track measurements optimally interpolated on a regular 1/4° grid by AVISO. By construction, the optimal interpolation filters many of the scales present in nature and is therefore not 100% representative of the observations on space scales less than 150 km (due do measurement noise and errors) and time scales less than 10 days (repeat cycle of the altimeters). In order to investigate the impact of the sub sampling and optimal interpolation on the EKE fields, the 1/50° model outputs were filtered to be more representative of the AVISO gridded outputs. To quantify the impact of the filtering, we compute the SSH wavenumber power spectrum in the 1/50° configuration over the 10° by 20° box shown in Figure 11. Over this energetic area, the 1/50° modeled power spectrum slope is k^{-5} in the 70-250 km mesoscale band (red in Fig. 13) and is representative of QG turbulence (see section 5 for a complete description of the power spectra distribution over the domain). Figure 13 illustrates the impact of the filtering on the wavenumber power spectrum. First, the subsampling of the model outputs to the 1/4° grid removes any information below 35 km (green in Fig.13). Time averaging the outputs over 10 days (dark blue in Fig. 13) or applying a 150 km band pass filter (turquoise in Fig.13) bring the power spectrum slope closer to AVISO (black in Fig. 13), but it is only when the two are applied together (purple in Fig. 13) that the modeled wavenumber spectrum resembles most closely that of AVISO. This result is consistent with Biri et al. (2016) who report that the spectrum derived from a 10 day resampled 4 km model follows more closely the altimeter spectrum due to aliasing (see also Arbic et al. (2013), who performed a similar exercise, but for spectral fluxes instead of spectra). Applying both the 10- day and 150 km band pass filters to the model outputs leads to EKE plots (Fig. 14) that resembles more closely the AVISO-derived EKE suggesting that the AVISO-derived EKE underestimates the observed EKE by approximately 30% in the Gulf Stream region. One should note, however, that even filtered, the modeled surface EKE is higher than observed south of the New England seamounts, suggesting that interactions with the topography may be overemphasized in the model.

4. Interior flows

Most model-data comparisons usually focus on the surface fields because of the scarcity of long time series at depth covering a large spatial area. Scott et al. (2010), expending on the work of Penduff et al. (2006) and Arbic et al. (2009), used a large collection of moored current meter records to assess the ability of three eddying global ocean models (POP, OCCAM, and HYCOM with 1/10° to 1/12° grid spacing), which resolve the first Rossby radius of deformation throughout most of the domain (i.e. up to 55-60°N), to simulate the time-averaged total kinetic energy throughout the water column. They found that the models agreed within a factor of two above 3500 m, and within a factor of three below 3500 m. Penduff et al. (2006) suggested that horizontal resolution was probably the most important factor limiting their 1/6° global model in generating realistic eddy kinetic energy, but Scott et al. (2010)'s results were not conclusive in that respect. Thoppil et al. (2011) did however find that increasing the model resolution to 1/25º significantly increased the surface and the abyssal EKE and clearly demonstrated that a better representation of upper ocean EKE is a prerequisite for strong eddy-driven abyssal circulation. In this section, we do show that horizontal resolution has a large impact on the distribution of interior kinetic energy by comparing the three simulations to eddy kinetic energy maps generated from moorings and floats.

In Figures 15 and 16, vertical sections of modeled zonal velocities and eddy kinetic energy along 55°W are compared to sections based on long term observations using drifters, floats, and moored current meters (Richardson, 1985). 55°W is perhaps one of the most observed section across the Gulf Stream with measurements first during POLYMODE (Richardson, 1985) and then during SYNOP (Bower and Hogg, 1996). In this region, most of the deep oceanic variability is generated by the surface currents via vortex stretching. It is very weak at 1/12°, in agreement with the Scott et al. (2010) results. But it does increases significantly at the model resolution is refined and, at 1/50°, the level and the pattern of the vertical zonal velocities and eddy kinetic energy resemble most closely the observations. This is consistent with Thoppil et al. (2011)'s statement that the surface and abyssal ocean circulation are strongly coupled through the energy cascades that vertically redistribute the energy and vorticity throughout the entire water column.

There are not that many spatial distributions of EKE at depths from observations. The few that exists are based on float measurements (SOFAR or Argo) and vary greatly in coverage and sampling. Figure 17 compares the modeled EKE distribution at 700 m to EKE derived from several years of SOFAR floats measurements (Richardson, 1993). As for the vertical sections, the 1/50° EKE distribution is closest to the observations, with a 1000 cm^2/s maximum west of the New England seamounts and an 800 cm^2/s extension past the seamounts. At 1000 m, the Argo floats data used by Ollitrault and Colin de Verdière (2014) to derive the EKE do not provide the fine temporal and spatial coverage of the SOFAR floats and the modeled 1/50° EKE differs significantly (Fig. 18). Filtering the modeled outputs over a 30-day time window and 100 km as for the Argo data leads to an EKE distribution that is much closer to the Ollitrault and Colin de Verdière (2014) map (Fig. 18a, c). As for the vertical sections, the magnitude of the 1/12° and 1/25° EKE distribution at 700 m and 1000 m are significantly less than in the 1/50° (Figs. 17,18).

5. Wavenumber spectra distribution

Wavenumber spectra are a useful tool to quantify the energy and variability associated with different scales and regions. In this section, we seek to address the questions of how robust is the modeled mesoscale and submesoscale eddy activity as a function of grid spacing and how representative is it of interior quasigeostrophic (QG) or surface quasigeostrophic (SQG) turbulence (Le Traon et al., 2008). The wavenumber spectra distribution is computed over the North Atlantic domain using boxes as in Le Traon et al. (1990), Paiva et al. (1999), Xu and Fu (2012), Richman et al. (2012), Sasaki and Klein (2012), and Dufau et al. (2016) among others. There is some sensitivity to the way spectra are computed and we follow Sasaki and Klein (2012) by making the box doubly periodic in both the zonal and meridional directions following Lapeyre (2009). Cosine tapered windows are also often used in the literature instead of the doubly periodic method (see for example Richman et al. (2012) which use a 10% cosine taper window) and in order to document the impact of the method, we compare in Figure 19 the spectra computed using several cosine taper windows (none, 5%, 10%, 20%, and 40%) and the doubly periodic approach. For a cosine taper window greater than 10%, the results are very close to the doubly periodic (or mirror) approach. The latter method is therefore preferred for its simplicity and reproducibility. The model outputs used to compute the spectra are daily averages, except when discussing the impact of internal waves and inertial motions where hourly snapshots are used.

Figure 20 displays the one-year SSH wavenumber spectra over the Gulf Stream energetic region (10° x 20° box defined in Figure 11) computed from daily averaged outputs of year 20 for the 1/12°, 1/25°, and 1/50°, respectively. Over the mesoscale range of 70 to 250 km, the slope does not vary as a function of the horizontal grid spacing and is $k^{-5.1}$, $k^{-4.9}$, and $k^{-5.0}$, respectively. It is now well documented that there is a strong seasonality associated with enhanced submesoscale activity in the winter mixed layer (Mensa et al., 2013; Sasaki et al., 2014; Callies et al., 2015; Rocha et al., 2016a). There is indeed a change in the slope of the SSH wavenumber spectra between summer and winter at all resolution for scales less than 70 km, but it is more pronounced at 1/12° than at 1/50° (Fig. 20). This does not mean that there is less small scales instabilities, just that the SSH signature of the high Rossby number submesoscale features is less pronounced in this high EKE region. The seasonality is clearly visible when comparing the relative vorticity distribution between summer and winter in Figures 21 and 22 and when computing the energy and vorticity spectra as in Figures 23 and 24. The difference in the number of small scale coherent features between the 1/12° and the 1/50° is striking, both in the summer and the winter (Figs. 21 and 22). But it is really at 1/50° that one can see an explosion of very small scale features during the winter months (Fig. 22; see also Fig. 1 of Sasaki et al. (2014)).

Figures 23 and 24 compare the wavenumber spectra for SSH, energy, and relative vorticity between two regions, the highly energetic Gulf Stream region (33°-43°N, 50°-70°W) as shown in Figure 11 and a low EKE region (20°-30°N, 20°-40°W). In the 70-250 km mesoscale range, the SSH wavenumber spectra slope is $k^{-4.2}$ in the low EKE region versus k^{-5} in the high EKE Gulf Stream region. This is consistent with the results put forward by Richman et al. (2012) and Sasaki and Klein (2012) which suggest that highly energetic regions are closer to QG turbulence and low energetic regions closer to SQG turbulence. Further examination of the SSH, energy and relative vorticity spectra (Figs. 21 and 22) in the two regions show additional differences. First, in the low EKE region, the SSH wavenumber spectra slope exhibits a stronger seasonal cycle than in the high EKE region which seems to indicate a stronger SSH signature of the smaller scale features in winter. Second, the kinetic energy wavenumber spectra in the high EKE region does not differ much when using either the total velocities or the geostrophic velocities. This is consistent with the results of section 3b which showed that the ageostrophic component forms small percentage of the total velocity. In the low EKE region, on the other hand, the wavenumber spectra slope in the mesoscale range is reduced by 25% when using geostrophic velocities to compute the spectra. Finally, the biggest difference is in the relative vorticity spectra which shows a stronger impact of the seasonal cycle in the low EKE region in the 70-250 km mesoscale range.

The spatial distribution of the SSH wavenumber spectra from altimeter observations shows a large spatial latitudinal variability with slopes closer to -5 at mid-latitudes and as high as -1 in the tropics (Xu and Fu, 2011, 2012; Zhou et al., 2015; Dufau et al., 2016). As in previously published modeling results (Paiva et al., 1999; Richman et al., 2012, Biri et al., 2016), we do not find this latitudinal dependence in the 70-250 km band (Fig. 25): the slope is everywhere between -5 and -4. Several explanations have been put forward to explain the discrepancy including aliasing and noise in the altimetry data (Biri et al., 2016), but it is also conceivable that one may underestimate the impact of high frequency motions such as internal waves and tides when using daily averages to compute the wavenumber spectra (Richman et al., 2012; Rocha et al., 2016b). In order to investigate the impact of fast moving features, the wavenumber spectra of Figure 25 were re-computed using hourly snapshots (Fig. 26). The biggest difference between daily and hourly spectra is in the tropics, mostly on scales below 70 km where the slopes can be as low as k^{-1}. The impact of fast moving features on the 70-250 km wavenumber range is much smaller, i.e. a decrease in the slope by up to 20% in a couple of 10° x 10° boxes (Fig. 26). Tides have been shown to have a significant impact on the wavenumber spectra on small scales (see Fig. 9 of Rocha et al. (2016b)), but does not appear to have an impact on the latitudinal dependence of the wavenumber spectra in numerical models (Richman et al., 2012).

6. Summary and conclusions

In this paper, we quantify the impact of horizontal resolution (1/12° to 1/50°; 6 to 1.5 km at mid-latitudes) on a series of identical North Atlantic experiments. First, we find that the representation of the Gulf Stream penetration and associated recirculating gyres shifts from unrealistic to realistic when the resolution is increased to 1/50°. This is consistent with results obtained by Hurlburt and Hogan (2000) using the 6-layer hydrodynamic NLOM model and by Levy et al. (2010) using the NEMO model in an idealized domain. In all cases, the non-linear effects of the submesoscale eddies that arise when the resolution reaches 1/50° intensifies the mid-latitude jet and increases its penetration eastward. Second, the penetration of the EKE into the deep ocean drastically increases with resolution and closely resembles the observations in the 1/50° configuration. And third, the wavenumber spectra are independent of horizontal resolution and latitudes in the 70-250 km mesoscale range.

Convergence studies such as this one where most parameters are not changed, except for the horizontal resolution, are unusual and the question arises as what one may expect as you continue to increase the horizontal resolution, decrease viscosity, and/or increase the order of the numerical schemes. At some point, for the right amount of internal dissipation and friction, the solution should settle at a level close to the observations. In this paper, we showed that the level of EKE in the 1/50° simulation was comparable to the observations when taking into account the aliasing associated with the altimeter sampling, but with one caveat: it was obtained by prescribing absolute winds at the ocean surface. While this is currently the norm for numerical models forced by an atmospheric reanalysis product, this does not allow any ocean feedback to the atmosphere. This feedback takes place via SST (see Small et al. (2008) for a review) and computation of the ocean current/wind shear (see Renault et al. (2016a) for a review). Earlier studies have shown that the latter can lead to a significant reduction of the surface EKE and Renault et al. (2016a) demonstrated that, using a coupled model, the current feedback deflects energy from the geostrophic current into the atmosphere and thus dampens eddies. Furthermore, the interaction of ocean eddies and the atmosphere regulates western boundary currents (Ma et al., 2016). In particular, Renault et al. (2016b) showed that the current feedback, through its “eddy killing” effect can stabilize the Gulf Stream separation, a prerequisite for a proper separation and penetration (Özgökmen et al., 1997). The reduction in surface EKE induced by the surface current feedback can be as high as 30%. This means that future numerical simulations will need to be able to exhibit higher level of EKE when using relative winds. As stated by Renault et al. (2016a), a bulk-forced oceanic uncoupled simulation should prescribe the surface stress using the relative wind in a bulk formulae which takes into account a parameterization of the partial re-energization of the ocean by the atmospheric response. Renault et al. (2016a) propose a surface stress computed with the wind relative to the current corrected by a current–wind coupling coefficient s_w as in $U = U_a - (1-s_w)U_a$. The value of the coefficient s_w are estimated to be between .2 and .3 and can vary spatially (R. Abel, personal communication).

In conclusion, it is fair to state that the next threshold for a significant improvement in western boundary currents representation (i.e. Gulf Stream in this paper) is an increase in the horizontal resolution from the eddying 1/10° to submesoscale enabled 1/50° grid spacing. Not only do the results presented in this paper support some of the results put forward by Hurlburt and Hogan (2000) and Levy et al. (2010), it also raises the question as the usefulness of intermediate resolutions such as 1/25° or 1/36°, at least for the Gulf Stream region. The computational cost of simulations at 1/50° is extremely large, and while currently available resources do not currently allow for all the sensitivity experiments to numerical choices, stress formulations, vertical resolution, tidal impact, etc., they will become more common in the future. Finally, we do realize that this paper is somewhat descriptive, but it sets the stage for in-depth analyses of water mass transformations and associated transports that will be presented in a companion paper.

Acknowledgements: EPC and XX are supported by the Office of Naval Research (Grant N00014-15-1-2594) and the NSF Physical Oceanography Program (Award 1537136). This work is a contribution to SWOT through the NASA grant NNX16AH79G. The authors thank M. Ollitrault and A. Colin de Verdière for providing the 1000 m float data used in Figure 18. They also thank B. Arbic, P. Klein, and two anonymous reviewers for their constructive comments. The numerical simulations were performed on supercomputers at the Navy DoD Supercomputing Resource Center, Stennis Space Center, Mississippi, using computer time provided by the U.S. DoD High Performance Computing Modernization Program.

References

Arbic, B.K., J.F. Shriver, P.J. Hogan, H.E. Hurlburt, J.L. McClean, E.J. Metzger, R.B. Scott, A. Sen, O.M. Smedstad, and A.J. Wallcraft, 2009: Estimates of bottom flows and bottom boundary layer dissipation of the oceanic general circulation from global high resolution models. *J. Geophys. Res.*, **114**, C02024.

Arbic, B.K., K.L. Polzin, R.B. Scott, J.G. Richman, and J.F. Shriver, 2013: On eddy viscosity, energy cascades, and the horizontal resolution of gridded satellite altimeter products. J. Phys. Oceanogr., 43, 283-289, doi:10.1175/JPO-D-11-0240.1.

Biri, S., N. Serra, M.G. Scharffenberg, and D. Stammer, 2016: Atlantic sea surface height and velocity spectra inferred from satellite altimetry and a hierarchy of numerical simulations. *J. Geophys. Res.*, **121**, 4157-4177.

Blaha, J., and B. Lunde, 1992: Calibrating altimetry to geopotenial anomaly and isotherm depths in the Western North Atlantic, *J. Geophys. Res.*, **97**, 7465-7477.

Bleck, R., 2002: An oceanic general circulation model framed in hybrid isopycnic-Cartesian coordinates. *Ocean Modelling*, **37**, 55–88.

Bower, A.S., and N.G. Hogg, 1996: Structure of the Gulf Stream and its recirculations at 55°W. *J. Phy. Oceanogr.*, **26**(6), 1002-1022.

Bryan, F.O., M.W. Hecht, and R.D. Smith, 2007: Resolution convergence and sensitivity studies with North Atlantic circulation models. Part I: The western boundary current system. *Ocean Modelling*, **16**, 141–159.

Capet, X., J.C. McWilliams, M.J. Molemaker, A.F. Shchepetkin, 2008: Mesoscale to sub-mesoscale transition in the California current system. Part I: flow structure, eddy flux, and observational tests. *J. Phys. Oceanogr*., **38**, 29–43.

Capet, X., G. Roullet, P. Klein, and G. Maze, 2016: Intensification of upper-ocean submesoscale turbulence through Charney baroclinic instability. *J. Phys. Oceanogr*., **46**, 33-65-3384.

Carnes, M.R., J.L.Mitchell, and P.W.Dewitt, 1990: Synthetic temperature profiles derived from GEOSAT altimetry - comparison with air-dropped expendable bathy-thermograph profiles. *J. Geophys. Res.*, **95**, 17,979-17,992.

Carnes, M.R., 2009: Description and evaluation of GDEM-V3.0. Naval Research Laboratory Memo. Rep. NRL/MR/7330–09-9165, 21 pp. [Available online at http://www7320.nrlssc.navy.mil/pubs/2009/carnes-2009.pdf.]

Callies, J., R. Ferrari, J.M. Klymak, and J. Gula, 2015: Seasonality in submesoscale turbulence, *Nat. Commun*., **6**, 6862, doi:10.1038/ncomms7862.

Chassignet, E.P., D.B. Olson, and D.B. Boudra, 1990: Motion and evolution of oceanic rings in a numerical model and in observations. *J. Geophys. Res.*, **95**, 22121-22140.

Chassignet, E. P., and Z. D. Garraffo, 2001: Viscosity parameterization and the Gulf Stream separation. In "*From Stirring to Mixing in a Stratified Ocean*", Proceedings 'Aha Huliko'a Hawaiian Winter Workshop, U. of Hawaii, January 15-19, 2001, P. Muller and D. Henderson, Eds., 37-41.

Chassignet, E.P., L.T. Smith, G.R. Halliwell, and R. Bleck, 2003: North Atlantic simulations with the hybrid coordinate ocean model (HYCOM): Impact of the vertical coordinate choice, reference pressure, and thermobaricity. *J. Phys. Oceanogr.*, **33**, 2504–2526.

Chassignet, E.P., H.E. Hurlburt, O.M. Smedstad, G.R. Halliwell, A.J. Wallcraft, E.J. Metzger, B.O. Blanton, C. Lozano, D.B. Rao, P.J. Hogan, and A. Srinivasan, 2006: Generalized vertical coordinates for eddy-resolving global and coastal ocean forecasts. *Oceanography*, **19**, 20-31.

Chassignet, E.P., and D.P. Marshall, 2008: Gulf Stream separation in numerical ocean models. In: *Ocean Modeling in an Eddying Regime*, Hecht, M., Hasumi, H. (Eds.), AGU Monograph Series, 39–62.

Chassignet, E.P., H.E. Hurlburt, E.J. Metzger, O.M. Smedstad, J. Cummings, G.R. Halliwell, R. Bleck, R. Baraille, A.J. Wallcraft, C. Lozano, H.L. Tolman, A. Srinivasan, S. Hankin, P. Cornillon, R. Weisberg, A. Barth, R. He, F. Werner, and J. Wilkin, 2009: U.S. GODAE: Global Ocean Prediction with the HYbrid Coordinate Ocean Model (HYCOM). *Oceanography*, **22**(2), 64-75.

CLIVAR Exchanges, 2014: Special issue on high resolution ocean climate modeling. No. **65** (Vol. 19 No. 2), 60 pp.

Douglass, E.M., and J.G. Richman, 2015: Analysis of ageostrophy in strong surface eddies in the Atlantic Ocean, *J. Geophys. Res*., **120**, 1490–1507, doi:10.1002/2014JC010350.

Dufau, C., M. Orsztynowicz, G. Dibarboure, R. Morrow, and P.-Y. Le Traon, 2016: Mesoscale resolution capability of altimetry: Present and future, *J. Geophys. Res*., **121**, doi:10.1002/2015JC010904.

Ezer, T. and G.L. Mellor, 2000: Sensitivity studies with the North Atlantic sigma coordinate Princeton Ocean Model. *Dynam. Atmos. Ocean.*, **32**, 185-208.

Fox-Kemper, B., R. Ferrari, and R., Hallberg, 2008: Parameterization of mixed layer eddies. Part I: Theory and diagnosis. *J. Phys. Oceanogr*., **38**, 1145–1165.

Griffies, S.M., A. Biastoch, C. Boening, F. Bryan, G. Danabasoglu, E.P. Chassignet, M.H. England, R. Gerdes, H. Haak, R.W. Hallberg, W. Hazeleger, J. Jungclaus, W.G. Large, G. Madec, A. Pirani, B.L. Samuels, M. Scheinert, A.S. Gupta, C.A. Severijns, H.L. Simmons, A.-M. Treguier, M. Winton, S. Yeager, and J. Yin, 2009: Coordinated Ocean-Ice Reference Experiments (COREs). *Ocean Modelling*, **26**, 1-46, doi:10.1016/j.ocemod.2008.08.007.

Grodsky, S.A., R. Lumpkin, and J.A. Carton, 2011: Spurious trends in global drifter currents. *Geophys. Res. Lett*., **38**, L10606, doi:10.1029/2011GL047393.

Hallberg, R., 2013: Using a resolution function to regulate parameterizations of oceanic mesoscale eddy effects. *Ocean Modelling*, **72**, doi:10.1016/j.ocemod.2013.08.007.

Haza, A.C., A.J. Mariano, T.M. Chin, and D.B. Olson, 2007: The mean flow and variability of the Gulf Stream slopewater system from MICOM. *Ocean Modelling*, **17**, 239-276.

Hurlburt, H. E., and P. J. Hogan, 2000: Impact of 1/8° to 1/64° resolution on Gulf Stream model-data comparisons in basin-scale subtropical Atlantic ocean models. *Dyn. Atmos. Oceans*, **32**, 283-329.

Kara, A.B., Wallcraft, A.J. and Hurlburt, H.E. 2005: A new solar radiation penetration scheme for use in ocean mixed layer studies: an application to the Black Sea using a fine resolution Hybrid Coordinate Ocean Model (HYCOM). *J. Phys. Oceanogr*., **35**, 13–32.

Klein, P., G. Lapeyre, G. Roullet, S. Le Gentil, and H. Sasaki, 2011: Ocean turbulence at meso and submesoscales: Connection between surface and interior dynamics, *Geophys. Astrophys. Fluid Dyn*., **105**, 421–437.

Lapeyre, G., 2009: What vertical mode does the altimeter reflect? On the decomposition in baroclinic modes and on a surface-trapped mode. *J. Phys. Oceanogr*., **39**, 2857-2874.

Large, W.G., J.C. McWilliams, and S.C. Doney, 1994: Ocean vertical mixing: a review and a model with a nonlocal boundary layer parameterization. *Rev. Geophys*., **32**, 363–403.

Le Traon, P.-Y., P. Klein, and B.-L. Hua, 2008: Do altimeter wavenumber spectra agree with the interior or surface quasigeostrophic theory? *J. Phys. Oceanogr*., **38**, 1137-1142.

Lévy M., P. Klein, A.-M. Tréguier, D. Iovino, G. Madec, S. Masson, and K. Takahashi, 2010: Modifications of gyre circulation by sub-mesoscale physics. *Ocean Modelling*, **34**, 1-15.

Ma, X., Z. Jing, P. Chang, X. Liu, R. Montuoro, R.J. Small, F.O. Bryan, R.J. Greatbatch, P. Brandt, D. Wu, X. Lin, and L. Wu, 2016: Western boundary currents regulated by interaction between ocean eddies and the atmosphere. *Nature*, **535**, 533–537. doi:10.1038/nature18640.

Maltrud, M.E., and J.L. McClean, 2005. An eddy resolving global 1/10° ocean simulation. *Ocean Modelling*, **8**, 31-54.

Marzocchi, A., J.J.-M. Hirschi, N.P. Holliday, S.A. Cunningham, A.T. Blaker, and A.C. Coward, 2015: The North Atlantic subpolar circulation in an eddy-resolving global ocean model. *J. Mar. Syst.*, **142**, 126–143, doi:10.1016/j.jmarsys.2014.10.007.

McCarthy, G. D., and coauthors, 2015: Measuring the Atlantic meridional overturning circulation at 26°N. *Prog. Oceanogr.*, **130**, 91–111, doi:10.1016/j.pocean.2014.10.006

Meinen, C.S., M.O. Baringer, and R.F. Garcia, 2010: Florida Current transport variability: An analysis of annual and longer-period signals. *Deep Sea Res.*, **57**, 835–846.

Mensa, J.A., Z. Garraffo, A. Griffa, T.M. Özgökmen, A. Haza, and M. Veneziani, 2013: Seasonality of the submesoscale dynamics in the Gulf Stream region, *Ocean Dyn.*, **63**, 923–941.

Niiler, P.N. N.A. Maximenko, and J. C. McWilliams, 2003: Dynamically balanced absolute sea level of the global ocean derived from near-surface velocity observations. *Geophys. Res. Lett.* **30**, doi:10.1029/2003GL018628.

Ollitrault, M. and A. Colin de Verdière, 2014: The ocean general circulation near 1000 m depth. *J. Phys. Oceanogr*, **44**, 384-408.

Oschlies, A., 2002: Improved representation of upper-ocean dynamics and mixed-layer depths in a model of the North Atlantic on switching from eddy-permitting to eddy-resolving grid resolution. *J. Phys. Oceanogr.*, **32**, 2277-2298.

Özgökmen, T. M., E. P. Chassignet, and A. M. Paiva, 1997: Impact of wind forcing, bottom topography, and inertia on midlatitude jet separation in a quasigeostrophic model. *J. Phys. Oceanogr.*, **27,** 2460-2476.

Paiva, A.M., J.T. Hargrove, E.P. Chassignet, and R. Bleck, 1999: Turbulent behavior of a fine mesh (1/12°) numerical simulation of the North Atlantic. *J. Mar. Sys.*, **21**, 307–320.

Penduff, T., B. Barnier, J.-M. Molines, and G. Madec, 2006: On the use of current meter data to assess the realism of ocean model simulations. *Ocean Modelling*, **11**, 399–416.

Renault, L., M.J. Molemaker, J.C. McWilliams, A.F. Shchepetkin, F. Lemarie, D. Chelton, S. Illig, and A. Hall, 2016a: Modulation of wind work by oceanic current interaction with the atmosphere. *J. Phys. Oceanogr.*, **46**, 1685-1704.

Renault, L., M.J. Molemaker, J. Gula, S. Masson, and J.C. McWilliams, 2016b: Control and stabilization of the Gulf Stream by oceanic current interaction with the atmosphere. *J. Phys. Oceanogr.*, **46**, 3439-3453.

Richman, J.G., B.K. Arbic, J.F. Shriver, E.J. Metzger, and A.J. Wallcraft, 2012: Inferring dynamics from the wavenumber spectra of an eddying global ocean model with embedded tides. *J. Geophys. Res.*, **117**, C12012, doi:10.1029/2012JC008364.

Richardson, P.L., 1985: Average velocity and transport of the Gulf Stream near 55°W. *J. Mar. Res.*, **43**, 83-111.

Richardson, P. L., 1993: A census of eddies observed in North Atlantic SOFAR float data. *Prog. Oceanog.*, **31**, 1-50.

Rio, M.-H., S. Guinehut, and G. Larnicol, 2011: New CNES-CLS09 global mean dynamic topography computed from the combination of GRACE data, altimetry, and in situ measurements, *J. Geophys. Res*., **116**, C07018, doi:10.1029/2010JC006505.

Rio, M.-H., S. Mulet, and N. Picot, 2014: Beyond GOCE for the ocean circulation estimate: Synergetic use of altimetry, gravimetry, and in situ data provides new insight into geostrophic and Ekman currents. *Geophys. Res. Lett*., **41**, 8918–8925, doi:10.1002/2014GL061773.

Rocha, C.B., S.T. Gille, T.K. Chereskin, and D. Menemenlis, 2016a: Seasonality of submesoscale dynamics in the Kuroshio Extension, *Geophys. Res. Lett*., **43**, 11,304-11,311, doi:10.1002/2016GL071349.

Rocha, C.B., T.K. Chereskin, S.T. Gille, and D. Menemenlis, 2016b: Mesoscale to submesoscale wavenumber spectra in Drake Passage, *J. Phys. Oceanogr*., **46**, 601-620.

Rossby T., C. Flagg and K. Donohue, 2010: On the variability of Gulf Stream transport from seasonal to decadal timescales. *J. Mar. Res*., **68**, 503–522.

Rossby, T., C. Flagg, K. Donohue, A. Sanchez-Franks, and J. Lillibridge, 2014: On the long-term stability of Gulf Stream transport based on 20 years of direct measurements, *Geophys. Res. Lett*., **41**, 114–120, doi:10.1002/2013GL058636.

Roullet, G., J.C. McWilliams, X. Capet and M.J. Molemaker, 2012: Properties of equilibrium geostrophic turbulence with isopycnal outcropping. *J. Phys. Oceanogr*., **42**, 18-38, 2012.

Saha, S., and co-authors, 2010: The NCEP Climate Forecast System Reanalysis. *Bull. Amer. Meteor. Soc*., **91**, 1015-1057.

Sasaki, H. and P. Klein, 2012: SSH Wavenumber spectra in the North Pacific from a high-resolution realistic simulation. *J. Phys. Oceanogr*., **42**, 1233–1241, doi: 10.1175/JPO-D-11-0180.1.

Sasaki, H., P. Klein, B. Qiu, and Y. Sasai, 2014: Impact of oceanic-scale interactions on the seasonal modulation of ocean dynamics by the atmosphere, *Nat. Commun*., **5**, 5636, doi:10.1038/ncomms6636.

Scott, R.B., B.K. Arbic, E.P. Chassignet, A.C. Coward, M. Maltrud, A. Srinivasan, and A. Varghese, 2010: Total kinetic energy in four global eddying ocean circulation models and over 5000 current meter records. *Ocean Modelling*, **32**, 157-169, doi:10.1016/j.ocemod.2010.01.005.

Small, R.J., S.P. deSzoeke, S.P. Xie, L. O'Neill, H. Seo, Q. Song, P. Cornillon, M. Spall, and S. Minobe, 2008: Air–sea interaction over ocean fronts and eddies. *Dyn. Atmos. Oceans*, **45**, 274–319.

Smith, R.D., M.E. Maltrud, F.O. Bryan, and M.W. Hecht, 2000: Numerical simulation of the North Atlantic Ocean at 1/10°. *J. Phys. Oceanogr*., **30**, 1532–1561.

Smith, W.H.F., and D.T. Sandwell, 1997: Global sea floor topography from satellite altimetry and ship depth soundings. *Science*, **277**, 1956–1962.

Soufflet, Y., P. Marchesiello, F. Lemarié, J. Jouanno, X. Capet, L. Debreu, and R. Benshila, 2016: On effective resolution in ocean models. *Ocean Modelling*, **98**, 36–50, doi:10.1016/j.ocemod.2015.12.004.

Teague, W.J., M.J. Carron, and P.J. Hogan, 1990: A comparison between the generalized digital environmental model and Levitus climatologies. *J. Geophys. Res*., **95**, 148-227, doi: 10.1029/89JC03682.

Thomas, L.N., A. Tandon, and A. Mahadevan, 2008: Sub-mesoscale processes and dynamics. *Ocean Modeling in an Eddying Regime*, Hecht, M., Hasumi, H. (Eds.), AGU Monograph Series, 17-38.

Thoppil, P.G., J.G. Richman and P.J. Hogan, 2011: Energetics of a global ocean circulation model compared to observations. *Geophys. Res. Lett*., **38**, L15607, doi:10.1029/2011GL048347.

Uppala, S.M., and Coauthors, 2005: The ERA-40 Re-Analysis. *Quart. J. Roy. Meteor. Soc*., **131**, 2961–3012, doi:10.1256/qj.04.176.

Xu, X., W. J. Schmitz Jr., H.E. Hurlburt, P.J. Hogan, and E.P. Chassignet, 2010: Transport of Nordic Seas overflow water into and within the Irminger Sea: An eddy-resolving simulation and observations. *J. Geophys. Res*., **115**, C12048, doi:10.1029/2010JC006351.

Xu, X., W.J. Schmitz Jr., H.E. Hurlburt, and P.J. Hogan, 2012: Mean Atlantic meridional overturning circulation across 26.58N from eddy-resolving simulations compared to observations. *J. Geophys. Res*., **117**, C03042, doi:10.1029/2011JC007586.

Xu, X., H.E. Hurlburt, W.J. Schmitz Jr., R.J. Zantopp, J. Fischer, and P.J. Hogan, 2013: On the currents and transports connected with the Atlantic meridional overturning circulation in the subpolar North Atlantic. *J. Geophys. Res.*, **118**, 502–516, doi:10.1002/jgrc.20065.

Xu, X., E.P. Chassignet, W.E. Johns, W.J. Schmitz Jr., and E.J. Metzger, 2014: Intraseasonal to interannual variability of the Atlantic meridional overturning circulation from eddyresolving simulations and observations. *J. Geophys. Res.*, **119**, 5140–5159, doi:10.1002/2014JC009994.

Xu, X., P.B. Rhines, E.P. Chassignet, and W.J. Schmitz Jr., 2015: Spreading of the Denmark Strait overflow water in the western subpolar North Atlantic: Insights from eddy-resolving simulations with a passive tracer. *J. Phys. Oceanogr*., **45**, 2913–2932, doi:10.1175/JPO-D-14-0179.1.

Xu, X., P.B. Rhines, and E.P. Chassignet, 2016: Temperature-salinity structure of the North Atlantic circulation and associated heat and freshwater transports. *J. Climate*, **29**, 7723-7741, doi:10.1175/JCLI-D-15-0798.1.

Xu, Y., and L.-L. Fu, 2011: Global variability of the wavenumber spectrum of oceanic mesoscale turbulence. *J. Phys. Oceanogr*., **41**, 802-809, doi:10.1175/2010JPO4558.1.

Xu, Y., and L.-L. Fu, 2012: The effects of altimeter instrument noise on the estimation of the wavenumber spectrum of sea surface height, *J. Phys. Oceanogr*., **42**, 2229–2233, doi:10.1175/JPO-D-12-0106.1.

Zhou, X.-H., D.-P. Wang, and D. Chen, 2015: Global wavenumber spectrum with corrections for altimeter high-frequency noise. *J. Phys. Oceanogr*., **45**, 495-503.

Table 1. Viscosity and diffusion coefficients

	1/12º	1/25º	1/50º
Laplacian coefficient for momentum	20 m^2/s	10 m^2/s	10 m^2/s
Biharmonic diffusive velocity (V_4) for momentum	1 cm/s	1 cm/s	4 cm/s
Biharmonic diffusive velocity for layer thickness	1 cm/s	1 cm/s	4 cm/s
Laplacian diffusive velocity for tracers	0.5 cm/s	0.5 cm/s	1 cm/s

Figure Captions

Figure 1. *Model domain and bathymetry (in kilometers).*

Figure 2. *Time evolution of the domain-averaged kinetic energy (in cm^2s^{-2}) for the three numerical experiments (1/12°, 1/25°, and 1/50°, respectively). The thin and thick lines denote monthly and annual averages, respectively.*

Figure 3. *Time mean sea surface height (in cm) in the Gulf Stream region from a-b) the AVISO climatology CNES-CLS13 and CNES-CLS09, and c-e) the 1/50°, 1/25°, and 1/12° HYCOM simulations, respectively (years 16-20).*

Figure 4. *Kinetic energy (cm^2s^{-2}) of time mean surface geostrophic current based on a) the AVISO climatology CNES-CLS13, and b-d) the 1/50°, 1/25°, and 1/12° HYCOM simulations, respectively (years 16-20).*

Figure 5. *a) Topex-Poseidon tracks (#932523A in red) superimposed on the mean SSH (in cm) from Niiler et al. (2203), b) observed mean dynamic topography (in cm) along track #932523A derived from 1) the in-situ bathythermographic data, 2) the AVISO climatology CNES-CLS13 and CNES-CLS09, and 3) the 1/50°, 1/25°, and 1/12° HYCOM simulations, respectively (years 16-20).*

Figure 6. *a) Mean velocity section as measured by the Oleander (1993-2012) with shipboard ACDP (55 m depth). The horizontal bar corresponding to 1 m/s and 0.5 m/s for the variance ellipse (from Rossby et al., 2014); and b-d) mean velocity for the 1/50°, 1/25°, and 1/12° HYCOM simulations, respectively (years 16-20). The depth contours range from 1000 to 5000 meters (grey shading).*

Figure 7. *Sea surface height variability (in cm) in the Gulf Stream region, (a) based on AVISO (1993-2012) and (b-d) the 1/50°, 1/25°, and 1/12° HYCOM simulations, respectively (years 16-20).*

Figure 8. *Sea surface height variability (in cm) in the Gulf Stream region from three regional NLOM simulations at 1/16°, 1/32°, and 1/64° resolution (from Hurlburt and Hogan, 2000).*

Figure 9. *Eddy kinetic energy (EKE, in cm^2s^{-2}) in the Gulf Stream region computed from SSH-derived geostrophic velocities: a) AVISO (1993-2012) and b-d) the 1/50°, 1/25°, and 1/12° HYCOM simulations, respectively (years 16-20).*

Figure 10. *Eddy kinetic energy (EKE, in cm^2s^{-2}) difference between the EKE of the total current and the EKE of the geostrophic current. The negative contribution implies that the ageostrophic current is in opposite direction to the geostrophic current.*

Figure 11. *Ratio of ageostrophic current speed to the total current speed for the month of February of model year 20. The red 20°x10° box denotes the area shown in Figure 12.*

Figure 12. *Averaged ageostrophic velocity (in cm/s) for the month of February of model year 20 in the Gulf Stream extension region (red box in Figure 11), showing the background Ekman drift and anticyclonic flow in both the Warm Core Ring (WR) and Cold Core Ring (CR).*

Figure 13. *SSH power spectra in the energetic Gulf Stream extension region (red box in Figure 11) for the gridded ¼° AVISO (black line) and for the 1/50° HYCOM on its original grid (red), subsampled on the ¼° grid (green), 10-day average (blue), 150-km band pass (cyan), and combined 10-day average/150-km band pass (magenta).*

Figure 14. *Surface eddy kinetic energy (in cm^2s^{-2}) in the Gulf Stream region computed from SSH-derived geostrophic velocities, a) the ¼° AVISO, b) 1/50° HYCOM, c) 150-km band passed 1/50° HYCOM, and d) combined 10-day average/150-km band passed 1/50° HYCOM.*

Figure 15. *Vertical distribution of the modeled zonal velocity (cm/s) and eddy kinetic energy (cm^2s^{-2}) along 55°W for the 1/50°, 1/25°, and 1/12° simulations, respectively.*

Figure 16. *Vertical distribution of the observed zonal velocity (cm/s) and eddy kinetic energy (in cm^2s^{-2}) along 55°W based on current meter moorings and subsurface floats (from Richardson, 1985).*

Figure 17. *Horizontal distribution of eddy kinetic energy (in cm^2s^{-2}) at 700 meter from a) SOFAR float measurements (Richardson, 1993), and b-d) the 1/50°, 1/25°, and 1/12° HYCOM simulations, respectively (years 16-20).*

Figure 18. *Horizontal distribution of eddy kinetic energy (in cm^2s^{-2}) at 1000 meter from a) Argo float measurements (Ollitrault and Colin de Verdiere, 2014), b) the 1/50° simulation, c) the 1/50° simulation with 30-day and 1° filters, d) the 1/25° simulation, and e) the 1/12° simulation.*

Figure 19. *SSH power spectra computed over the 20°x10° red box in Figure 11 using mirror (black) and tapered cosine windows of different size (none, 5%, 10%, 20% and 40%). Results based on 1-year average (year 20) of the 1/50° simulation.*

Figure 20. *SSH power spectra in the energetic Gulf Stream region (the 20°x10° box in Figure 11) computed from daily averaged model outputs of year 20 for 1/12°, 1/25°, and 1/50° simulations. The black lines are annual mean; red and blue lines are average over summer and winter, respectively. The green dash line corresponds to k-5 and the shaded area brackets the 70-250 km mesoscale range.*

Figure 21. *A snapshot of dimensionless surface relative vorticity (ζ/f with $f=10^{-4}$ s^{-1}) in the Gulf Stream region in summer (August 31) and winter (March 1) of year 20 of the 1/12° simulation.*

Figure 22. *A snapshot of dimensionless surface relative vorticity (ζ/f with $f=10^{-4}$ s^{-1}) in the Gulf Stream region in summer (August 31) and winter (March 1) of year 20 of the 1/50° simulation.*

Figure 23. *Power spectra in the energetic Gulf Stream region (red box in Figure 11) computed from daily averaged outputs of year 20 for the 1/50° configuration: a) SSH, b) total surface velocity, c) SSH-derived geostrophic velocity, and d) surface relative vorticity. Annual, summer, and winter mean power spectra are denoted in black, red, and blue, respectively.*

Figure 24. *Power spectra in a less energetic northeast Atlantic region (20-30°N, 20-40°W, see Figure 25) computed from daily averaged outputs of year 20 for the 1/50° configuration: a) SSH, b) total surface velocity, c) SSH-derived geostrophic velocity, and d) surface relative vorticity. Annual, summer, and winter mean power spectra are denoted in black, red, and blue, respectively.*

Figure 25. *Sea-surface height power spectra slopes (in the 70-250 km mesoscale range) for 10x10° boxes, calculated from on daily mean outputs for model year 20 of the 1/50° configuration.*

Figure 26. *Sea-surface height power spectra for the 10x10° boxes shown in Figure 25, calculated from daily means (solid lines) and hourly snapshots (dashed lines) for the month of December of year 20 of the 1/50° simulation. The captions in each panel indicate the western-most longitude of the box and the corresponding spectral slopes in the 70-250 mesoscale range (daily and hourly).*

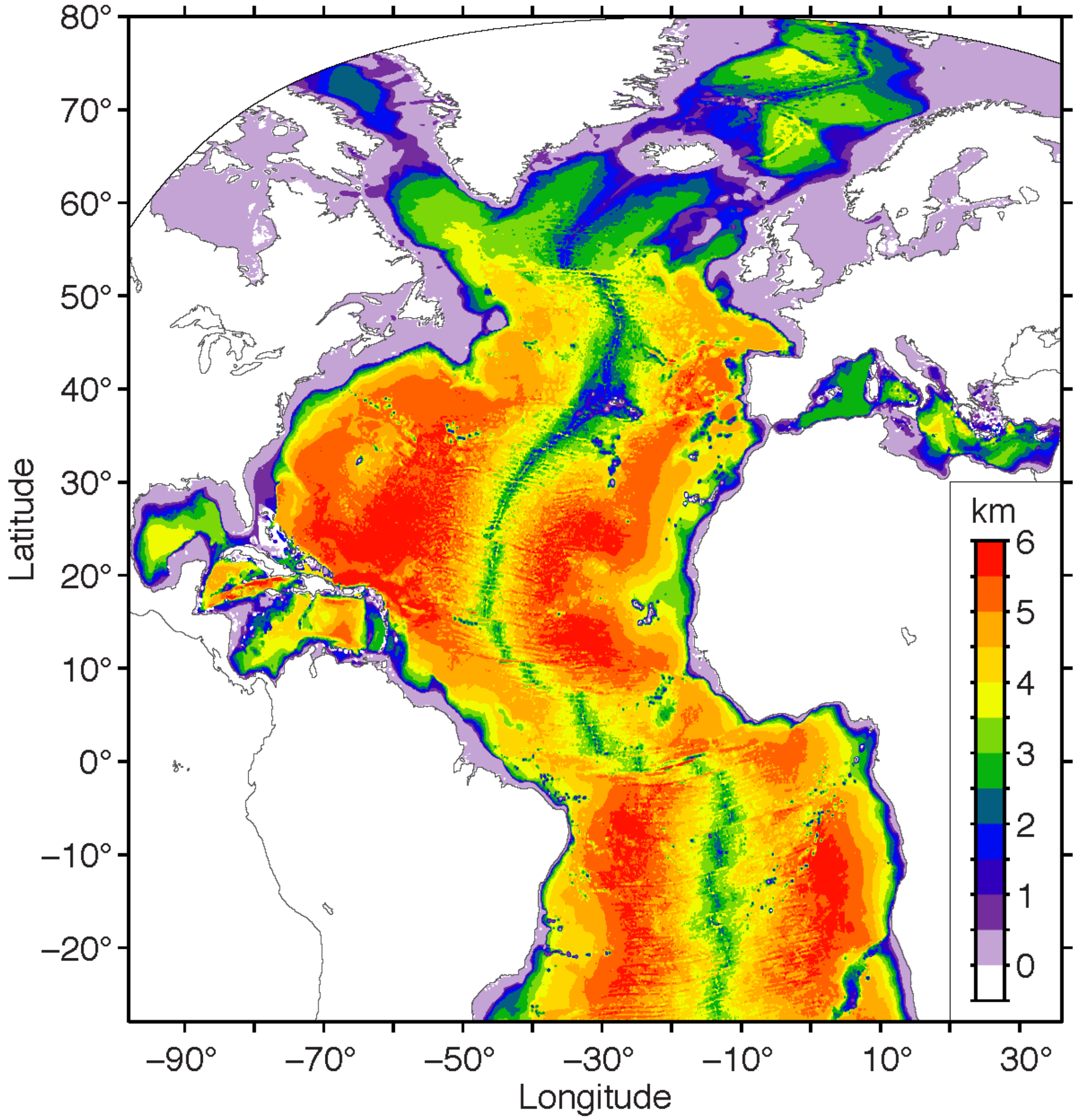

***Figure 1**. Model domain and bathymetry (in kilometers).*

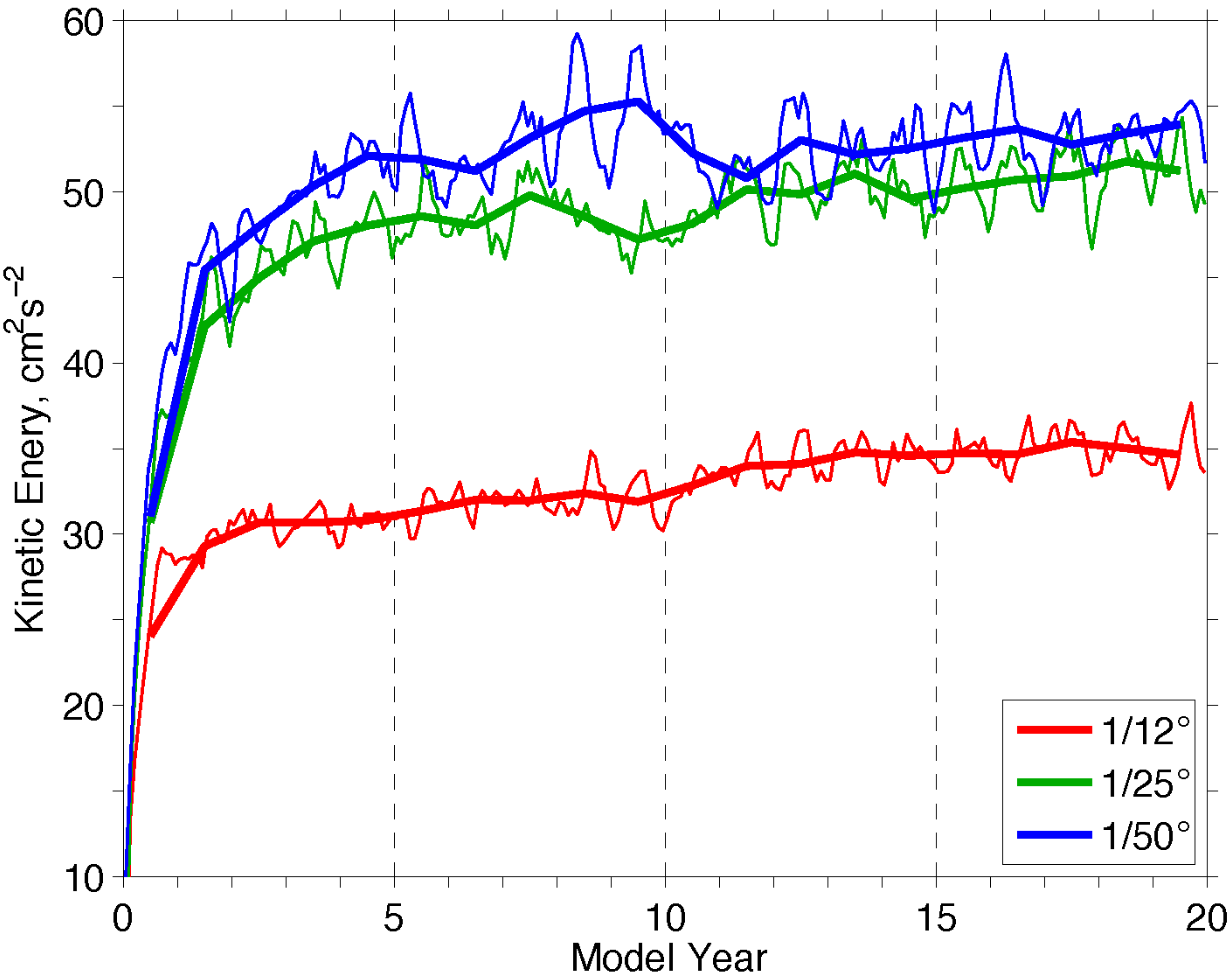

Figure 2. *Time evolution of the domain-averaged kinetic energy (in cm^{2}s^{-2}) for the three numerical experiments (1/12°, 1/25°, and 1/50°, respectively). The thin and thick lines denote monthly and annual averages, respectively.*

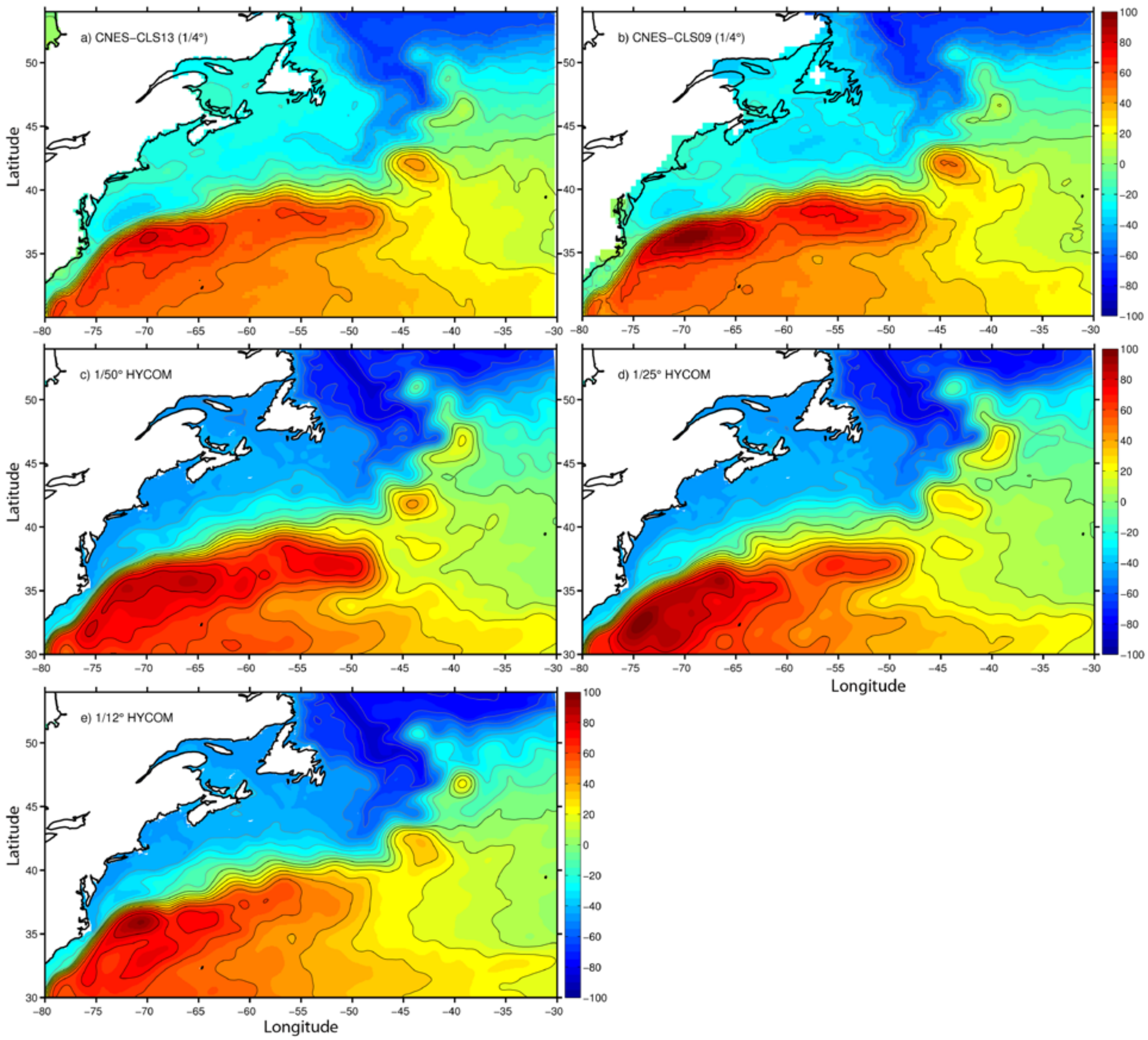

Figure 3. *Time mean sea surface height (in cm) in the Gulf Stream region from a-b) the AVISO climatology CNES-CLS13 and CNES-CLS09, and c-e) the 1/50°, 1/25°, and 1/12° HYCOM simulations, respectively (years 16-20).*

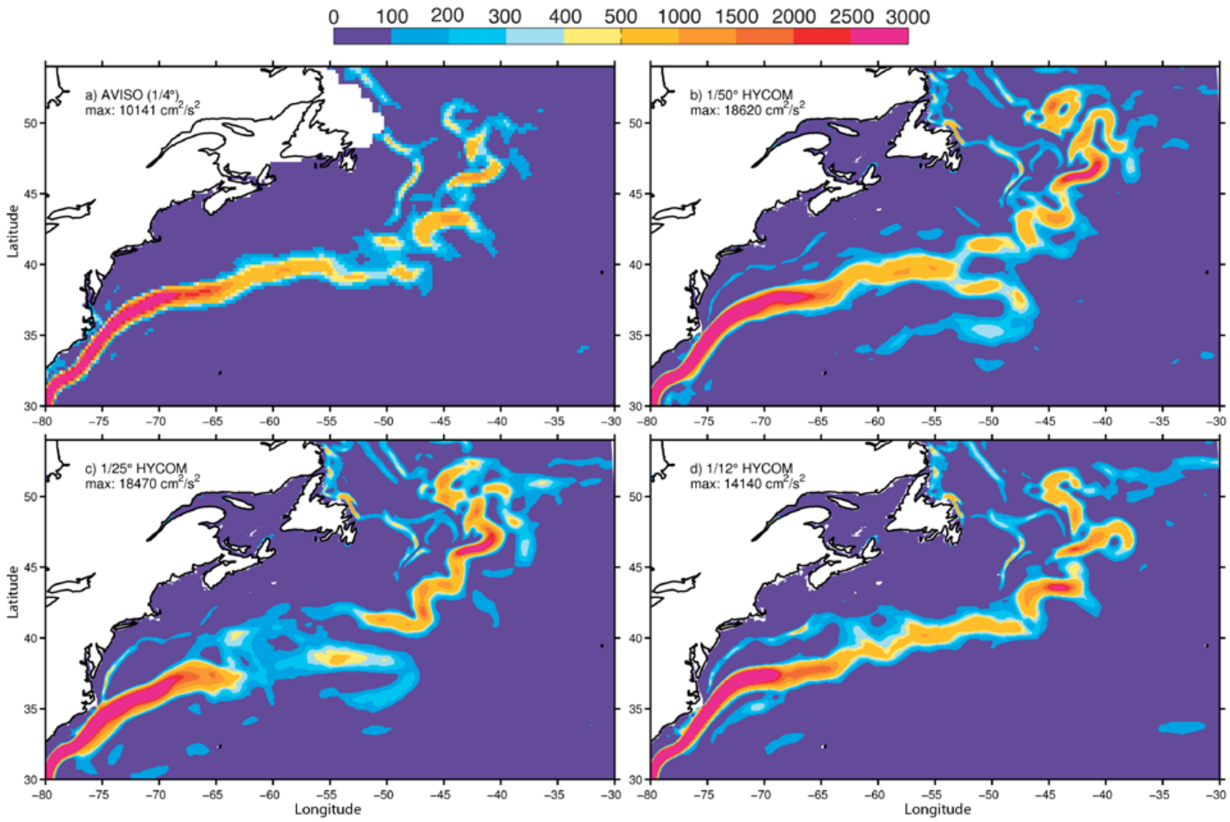

Figure 4. *Kinetic energy (cm^2s^{-2}) of time mean surface geostrophic current based on a) the AVISO climatology CNES-CLS13, and b-d) the 1/50°, 1/25°, and 1/12° HYCOM simulations, respectively (years 16-20).*

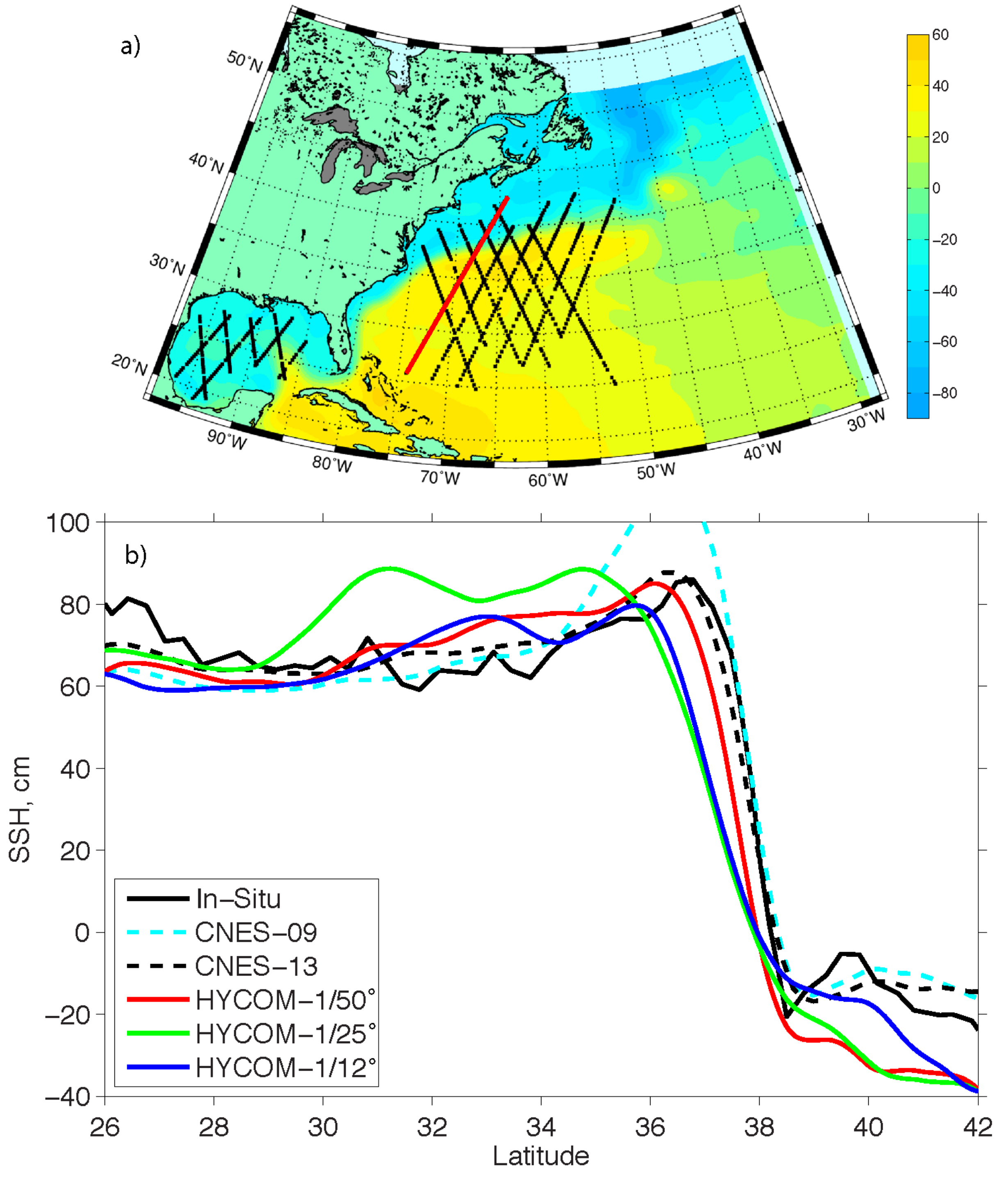

Figure 5. *a) Topex-Poseidon tracks (#932523A in red) superimposed on the mean SSH (in cm) from Niiler et al. (2203), b) observed mean dynamic topography (in cm) along track #932523A derived from 1) the in-situ bathythermographic data, 2) the AVISO climatology CNES-CLS13 and CNES-CLS09, and 3) the 1/50°, 1/25°, and 1/12° HYCOM simulations, respectively (years 16-20).*

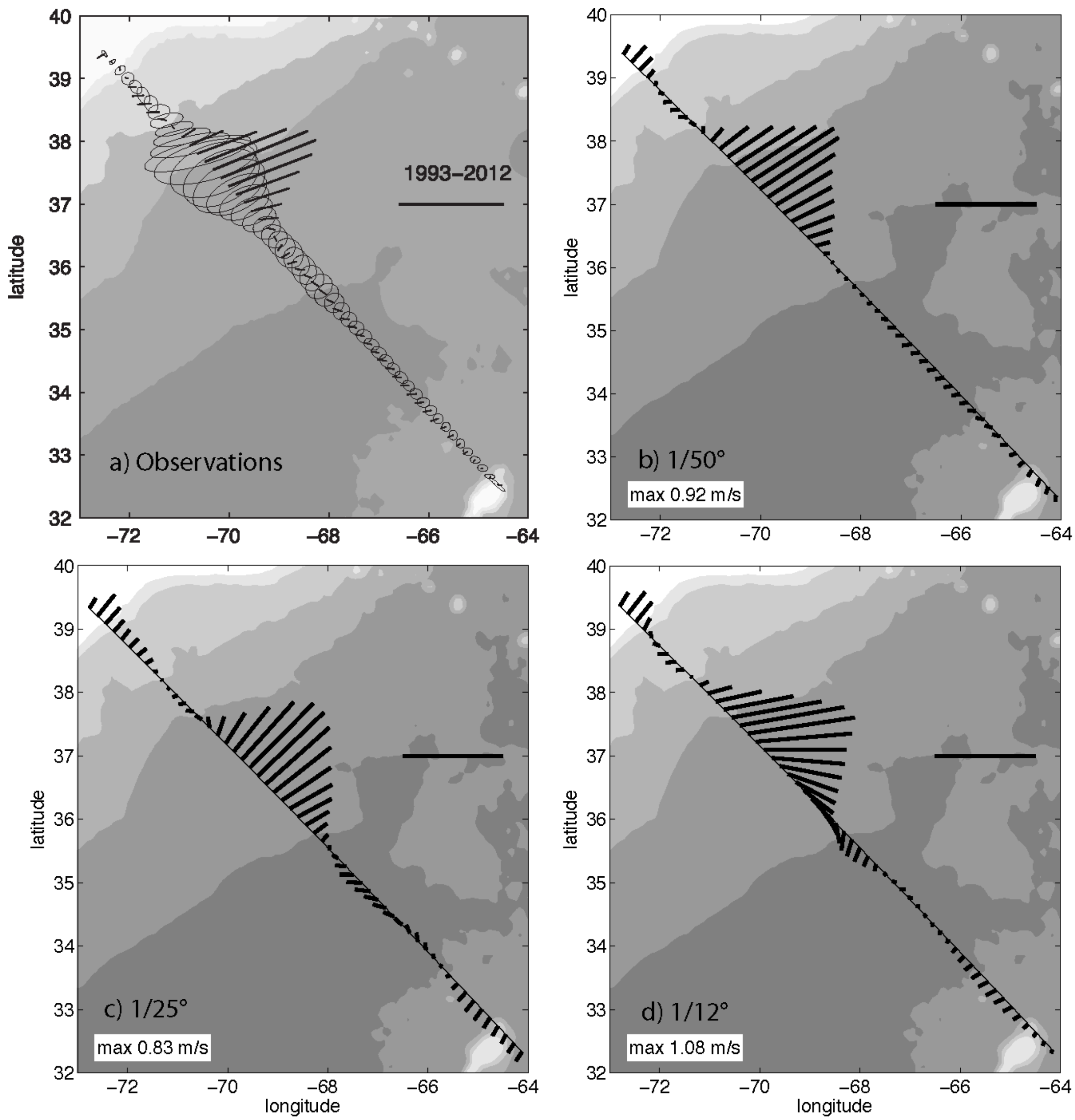

Figure 6. *a) Mean velocity section as measured by the Oleander (1993-2012) with shipboard ACDP (55 m depth). The horizontal bar corresponding to 1 m/s and 0.5 m/s for the variance ellipse (from Rossby et al., 2014); and b-d) mean velocity for the 1/50°, 1/25°, and 1/12° HYCOM simulations, respectively (years 16-20). The depth contours range from 1000 to 5000 meters (grey shading).*

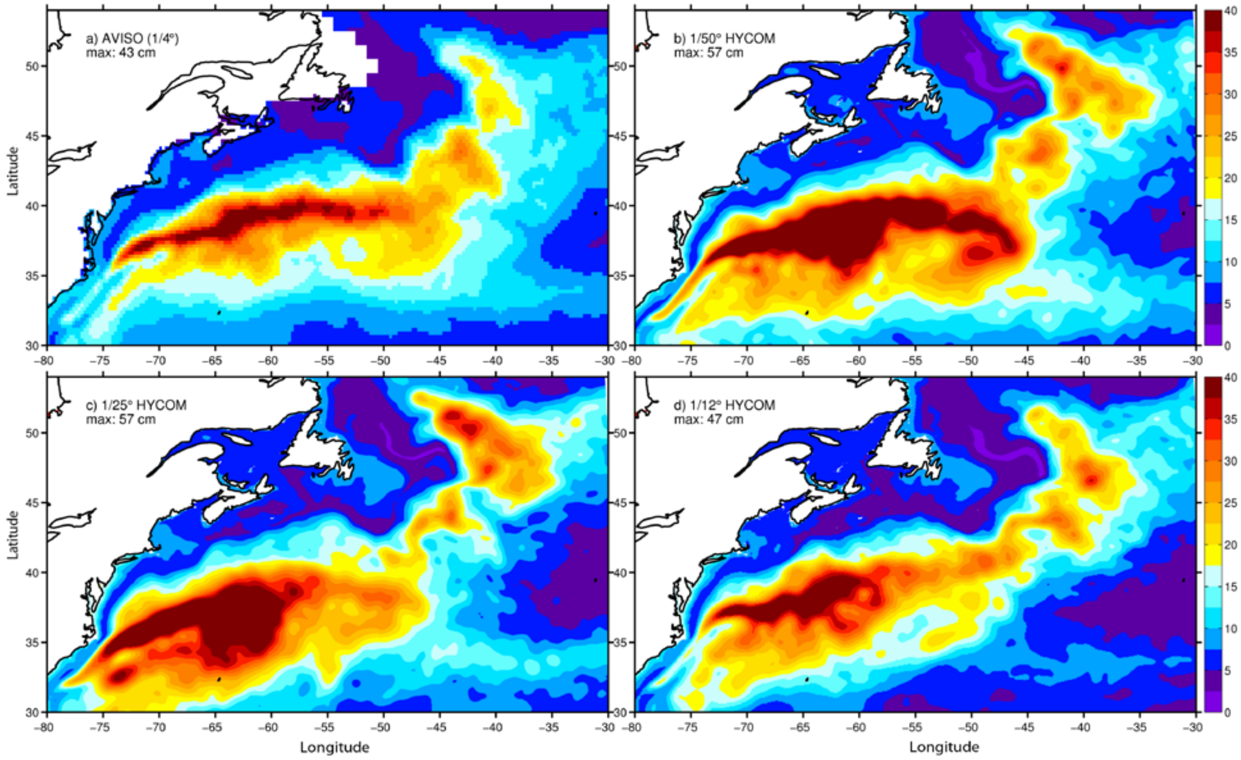

Figure 7. *Sea surface height variability (in cm) in the Gulf Stream region, (a) based on AVISO (1993-2012) and (b-d) the 1/50°, 1/25°, and 1/12° HYCOM simulations, respectively (years 16-20).*

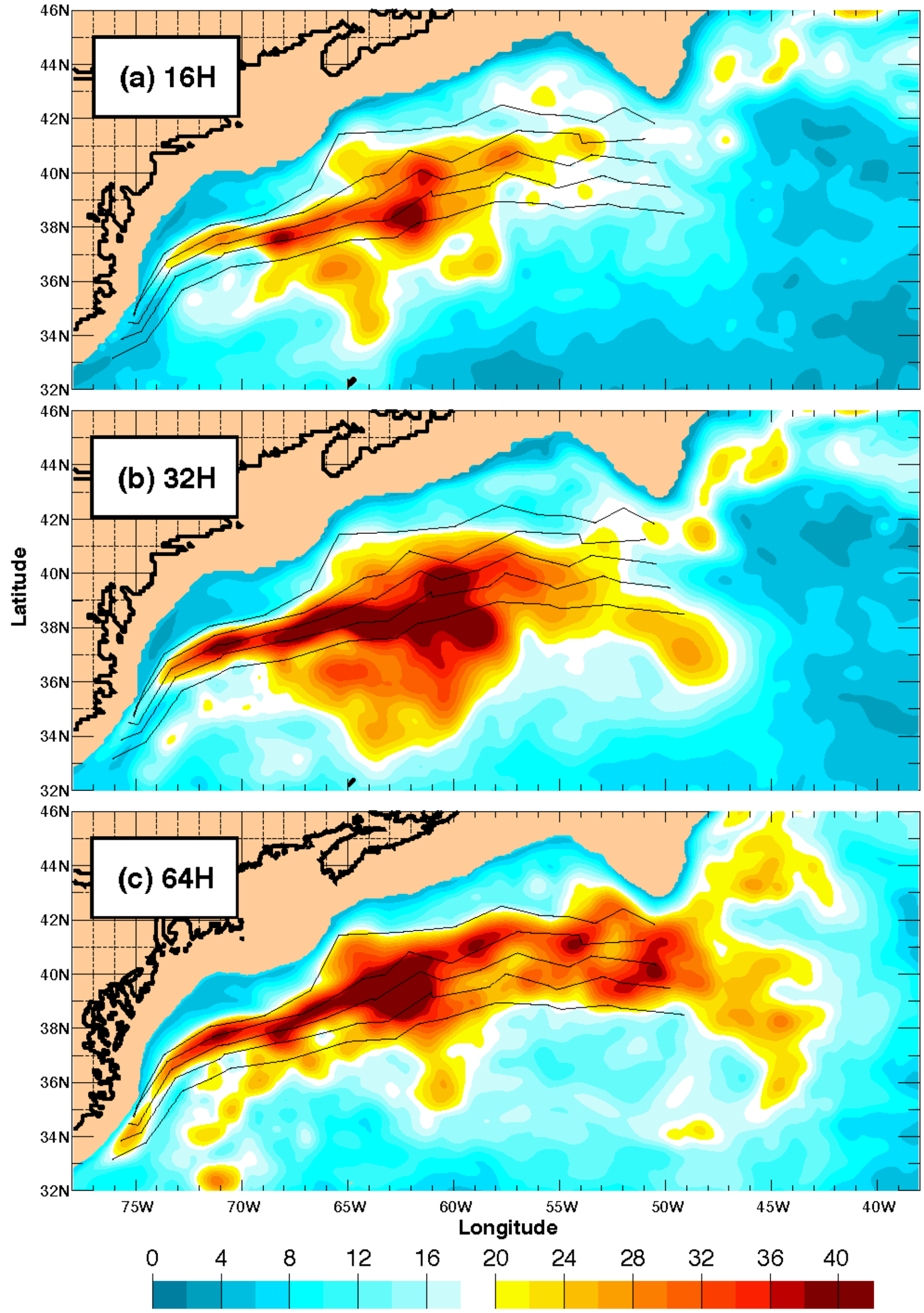

Figure 8. *Sea surface height variability (in cm) in the Gulf Stream region from three regional NLOM simulations at 1/16°, 1/32°, and 1/64° resolution (from Hurlburt and Hogan, 2000).*

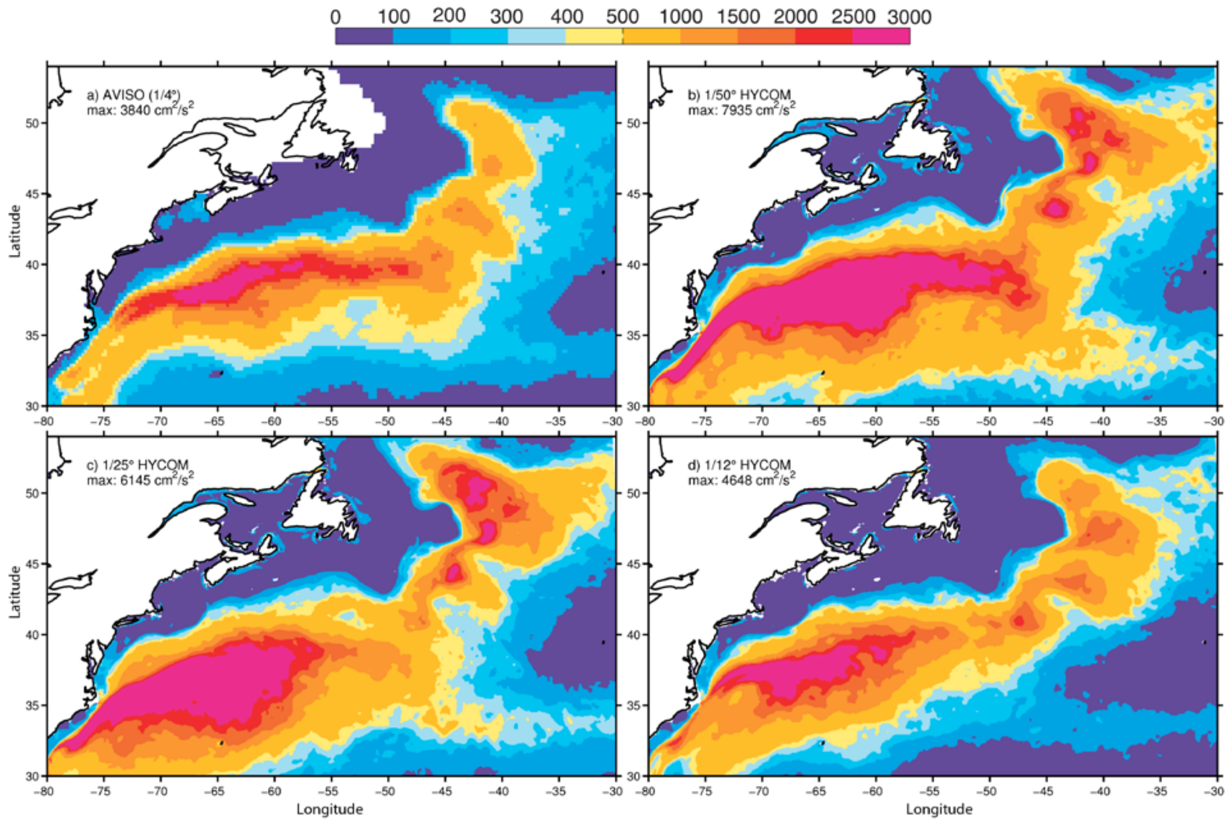

Figure 9. *Eddy kinetic energy (EKE, in cm^2s^{-2}) in the Gulf Stream region computed from SSH-derived geostrophic velocities: a) AVISO (1993-2012) and b-d) the 1/50°, 1/25°, and 1/12° HYCOM simulations, respectively (years 16-20).*

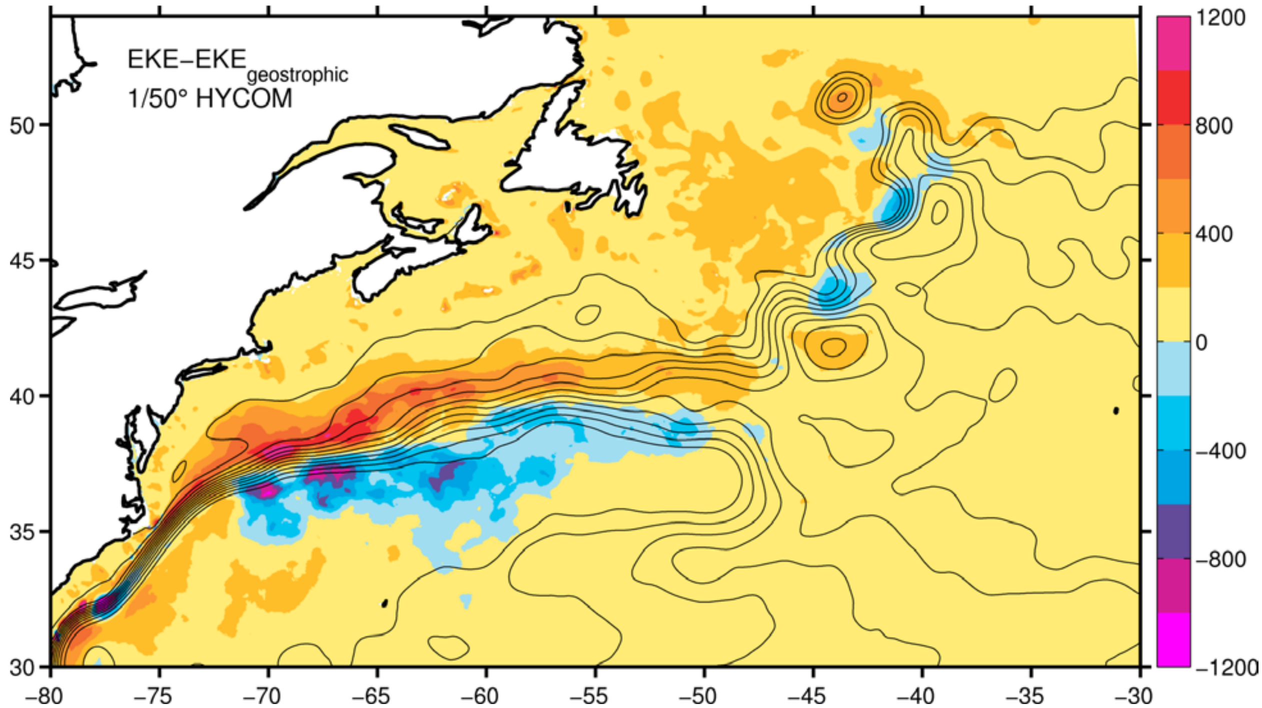

Figure 10. *Eddy kinetic energy (EKE, in cm^{2}s^{-2}) difference between the EKE of the total current and the EKE of the geostrophic current. The negative contribution implies that the ageostrophic current is in opposite direction to the geostrophic current.*

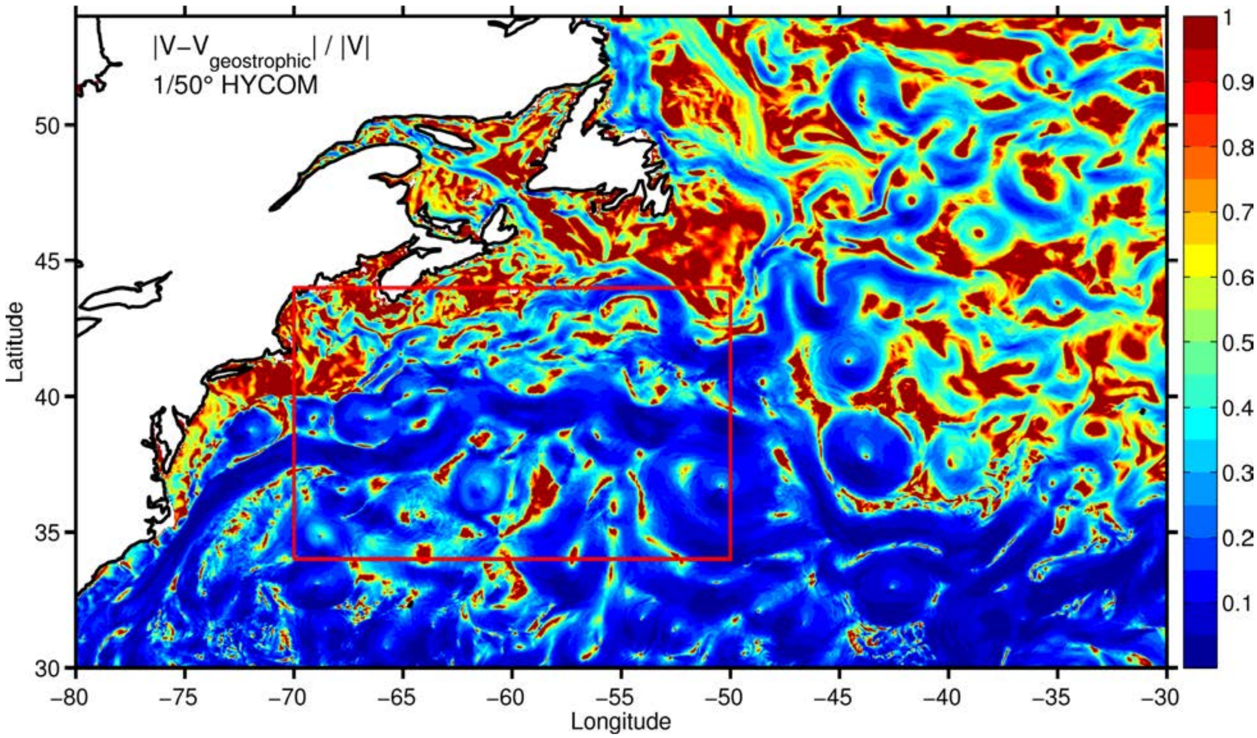

Figure 11. *Ratio of ageostrophic current speed to the total current speed for the month of February of model year 20. The red 20°x10° box denotes the area shown in Figure 12.*

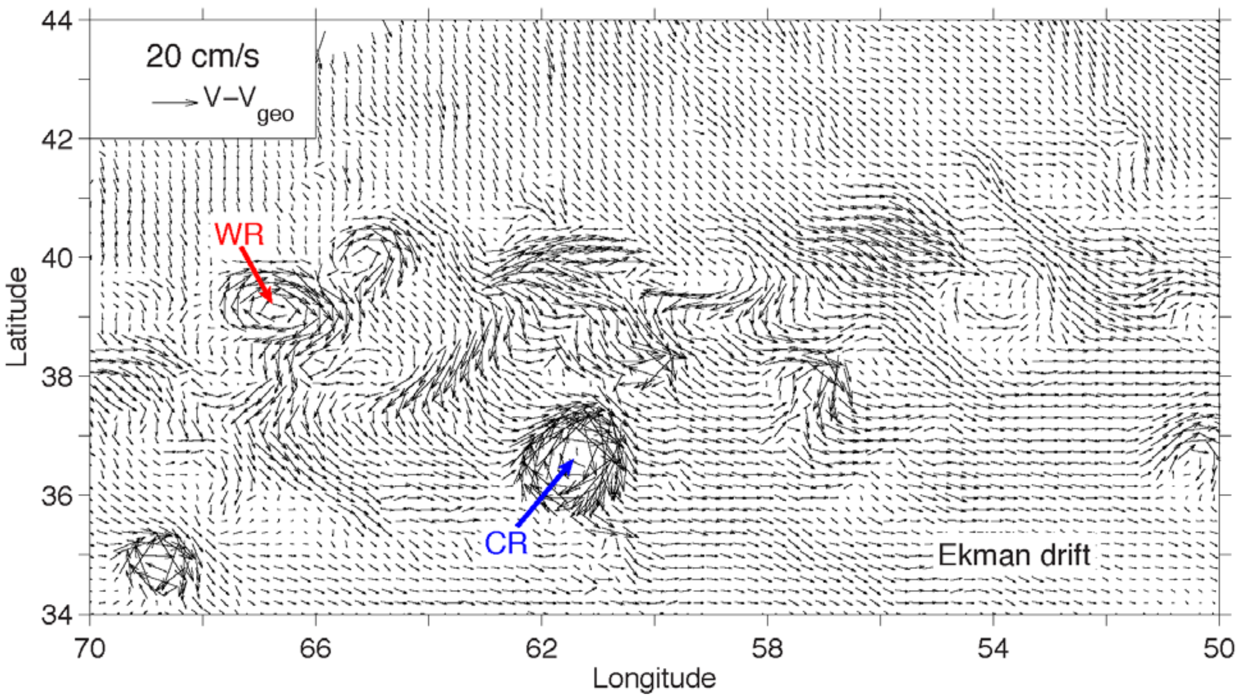

Figure 12. *Averaged ageostrophic velocity (in cm/s) for the month of February of model year 20 in the Gulf Stream extension region (red box in Figure 11), showing the background Ekman drift and anticyclonic flow in both the Warm Core Ring (WR) and Cold Core Ring (CR).*

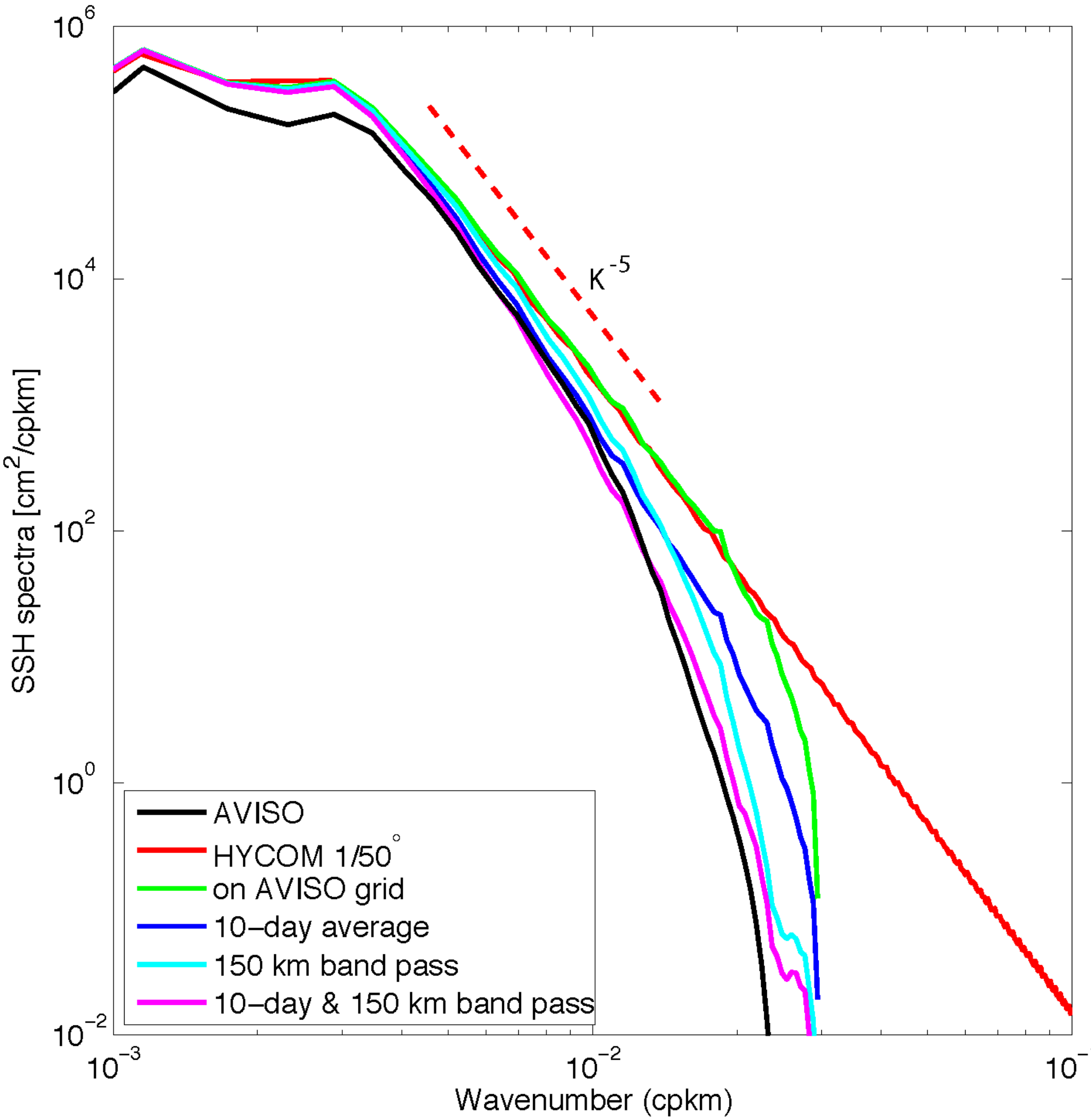

Figure 13. *SSH power spectra in the energetic Gulf Stream extension region (red box in Figure 11) for the gridded ¼° AVISO (black line) and for the 1/50° HYCOM on its original grid (red), subsampled on the ¼° grid (green), 10-day average (blue), 150-km band pass (cyan), and combined 10-day average/150-km band pass (magenta).*

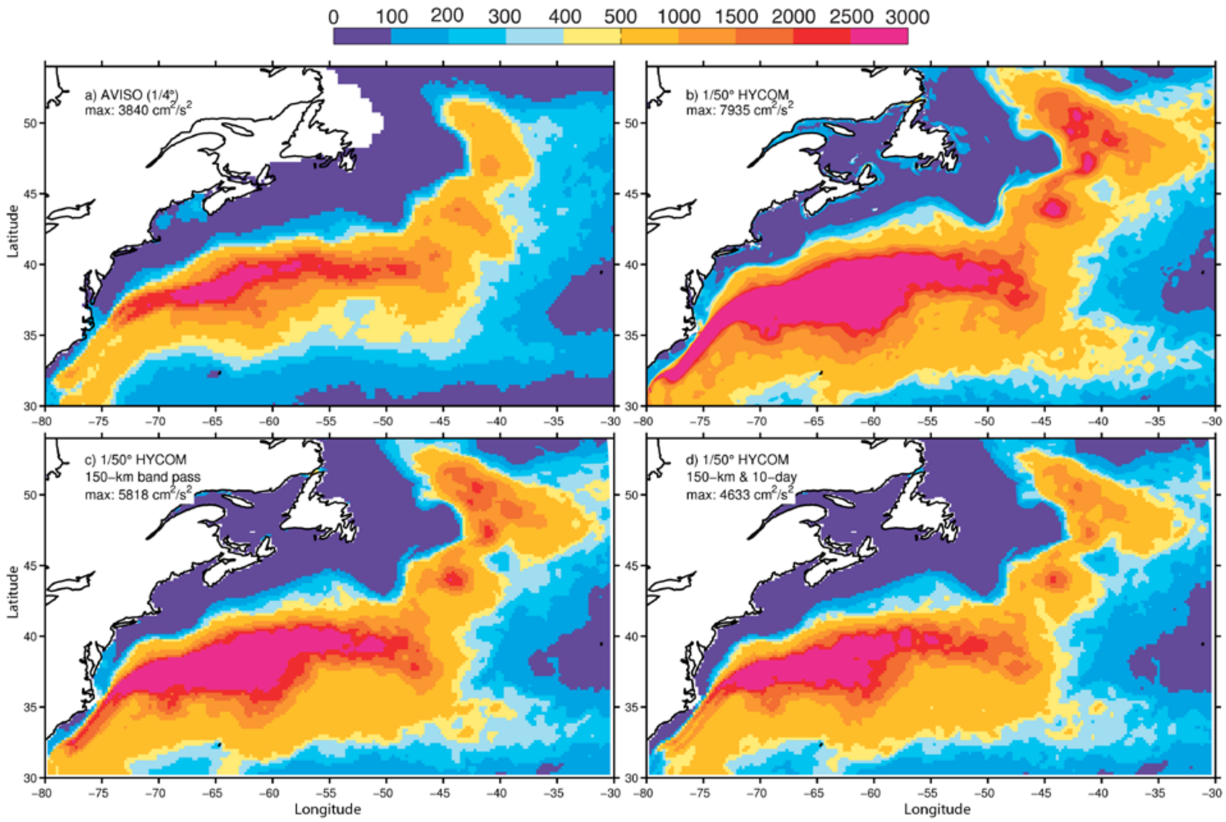

Figure 14. *Surface eddy kinetic energy (in* cm^2s^{-2}*) in the Gulf Stream region computed from SSH-derived geostrophic velocities, a) the ¼° AVISO, b) 1/50° HYCOM, c) 150-km band passed 1/50° HYCOM, and d) combined 10-day average/150-km band passed 1/50° HYCOM.*

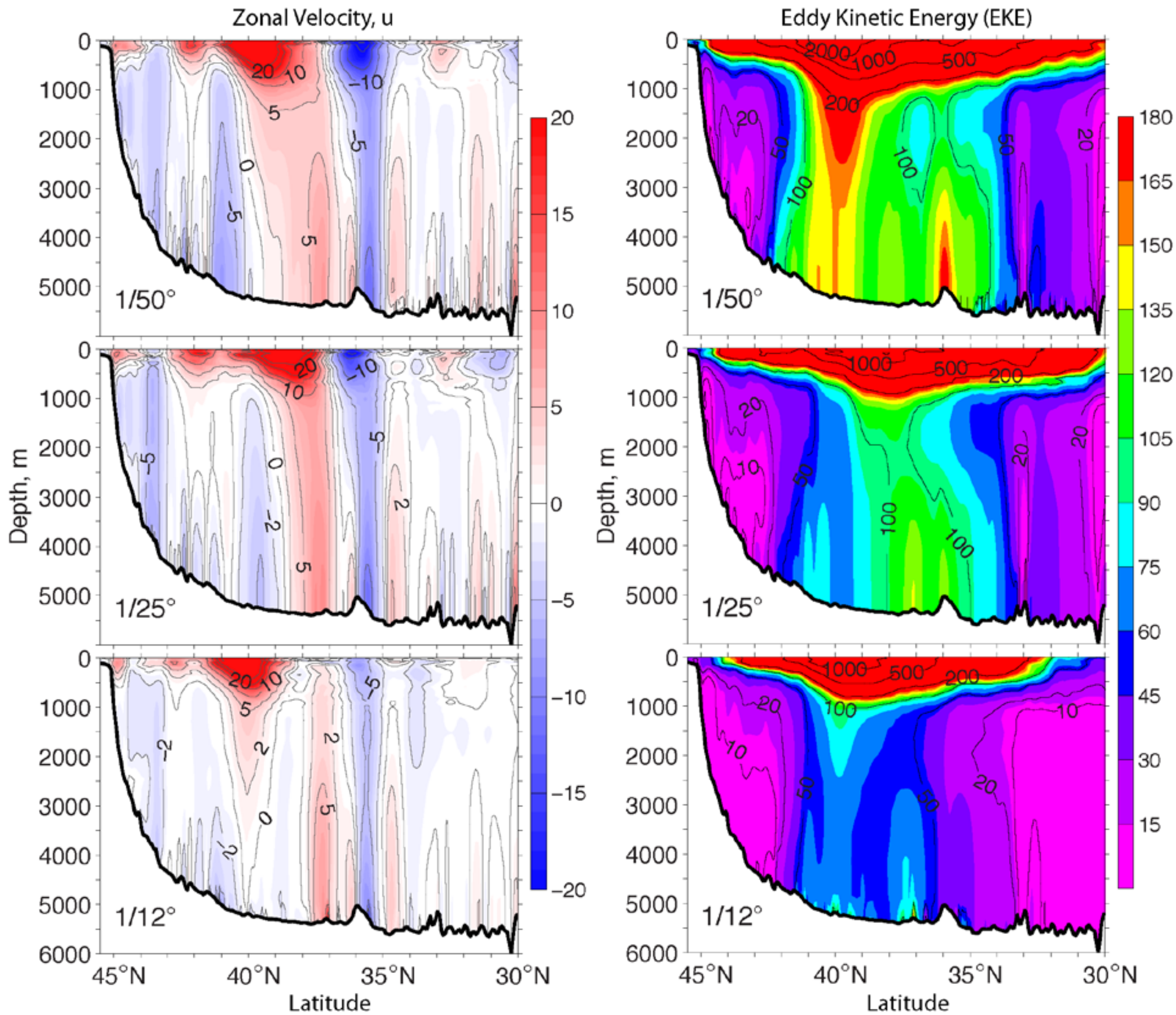

Figure 15. *Vertical distribution of the modeled zonal velocity (cm/s) and eddy kinetic energy (cm^{2}s^{-2}) along 55°W for the 1/50°, 1/25°, and 1/12° simulations, respectively.*

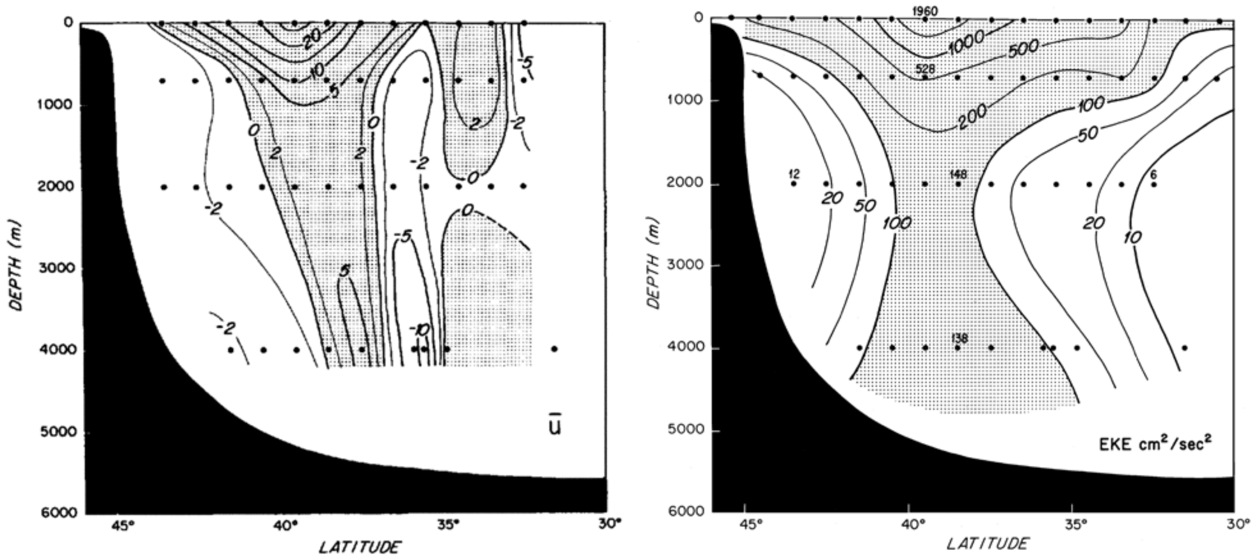

Figure 16. *Vertical distribution of the observed zonal velocity (cm/s) and eddy kinetic energy (in cm^{2}s^{-2}) along 55°W based on current meter moorings and subsurface floats (from Richardson, 1985).*

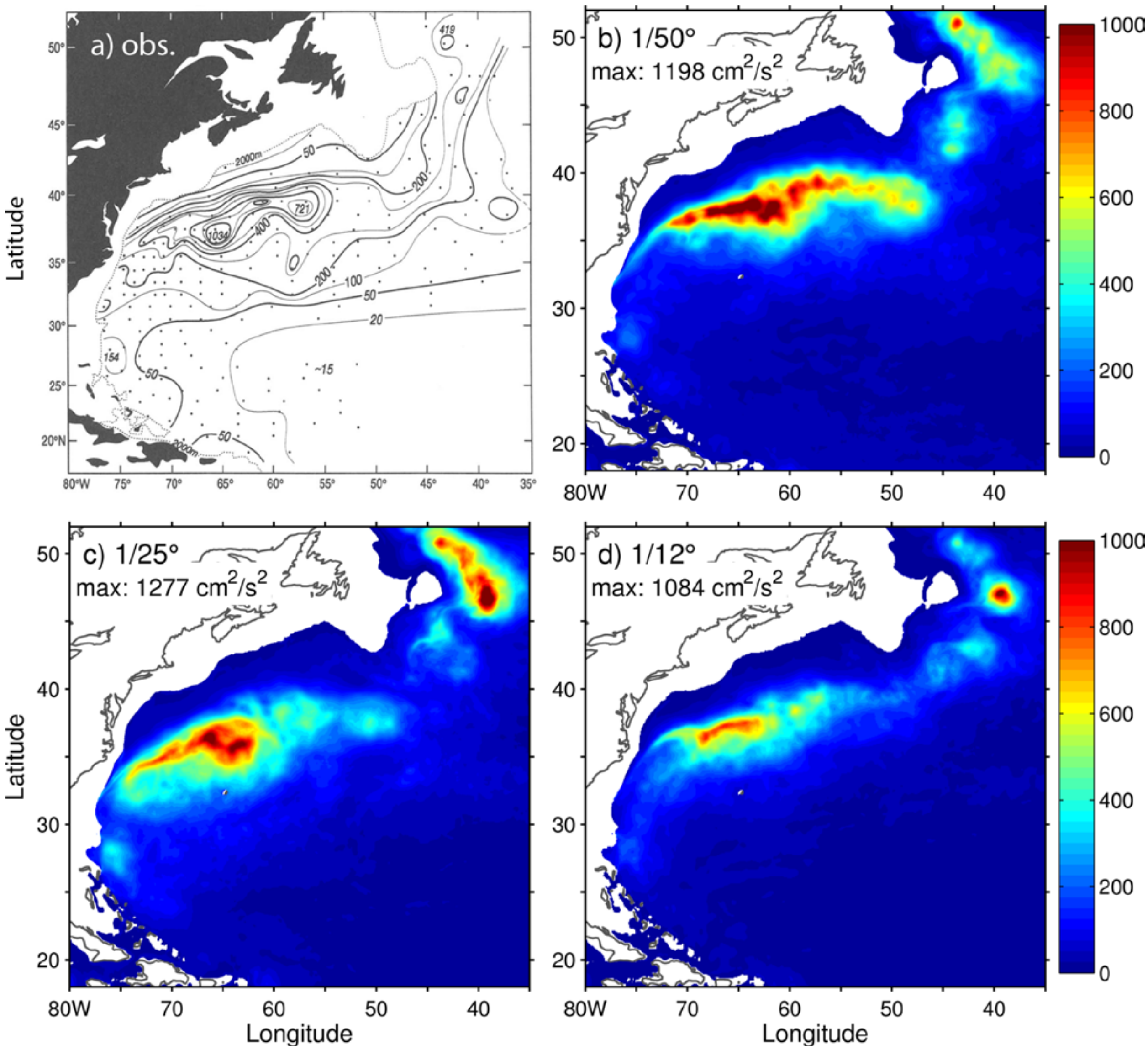

Figure 17. *Horizontal distribution of eddy kinetic energy (in cm^2s^{-2}) at 700 meter from a) SOFAR float measurements (Richardson, 1993), and b-d) the 1/50°, 1/25°, and 1/12° HYCOM simulations, respectively (years 16-20).*

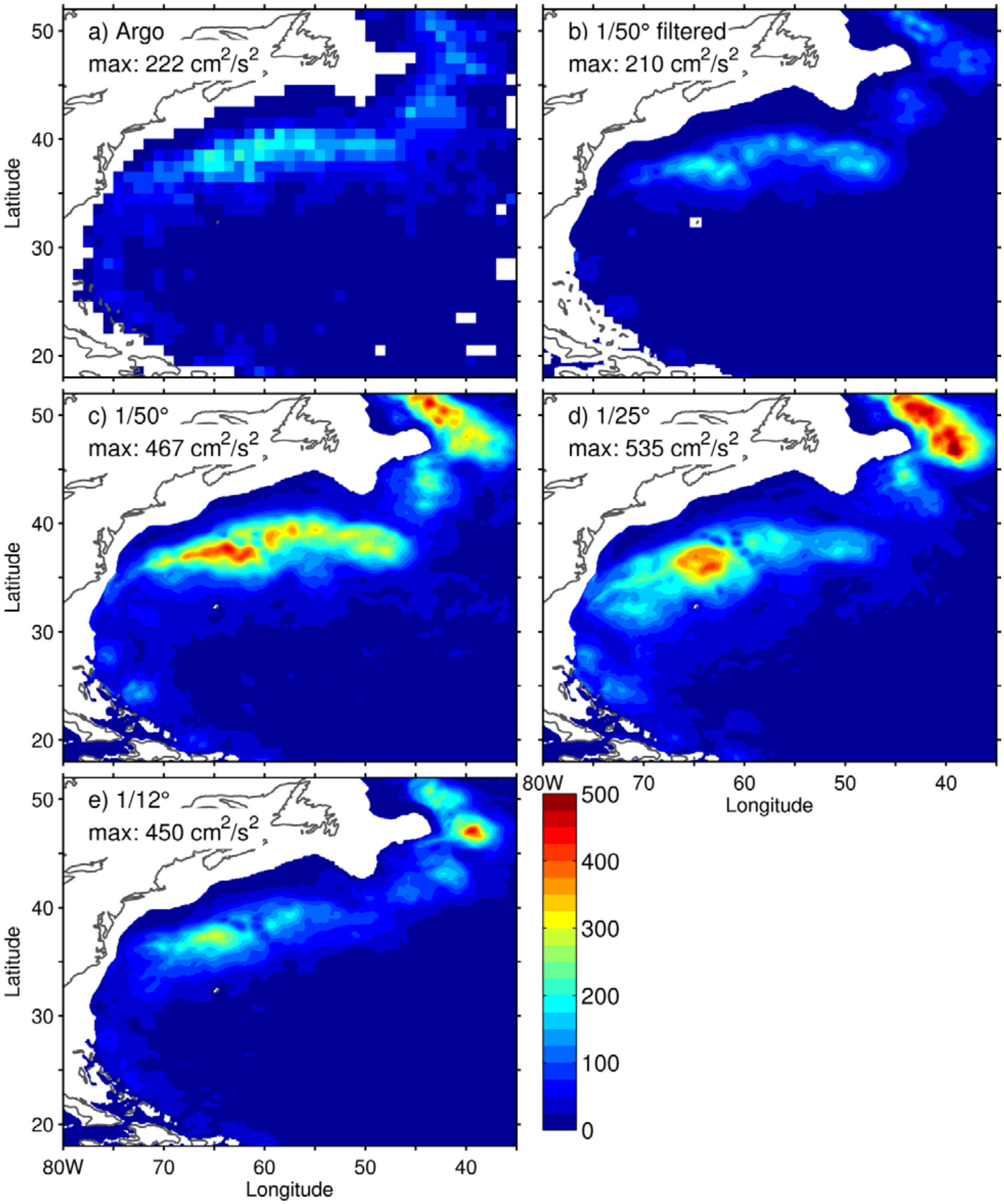

Figure 18. *Horizontal distribution of eddy kinetic energy (in cm^{2}s^{-2}) at 1000 meter from a) Argo float measurements (Ollitrault and Colin de Verdiere, 2014), b) the 1/50° simulation, c) the 1/50° simulation with 30-day and 1° filters, d) the 1/25° simulation, and e) the 1/12° simulation.*

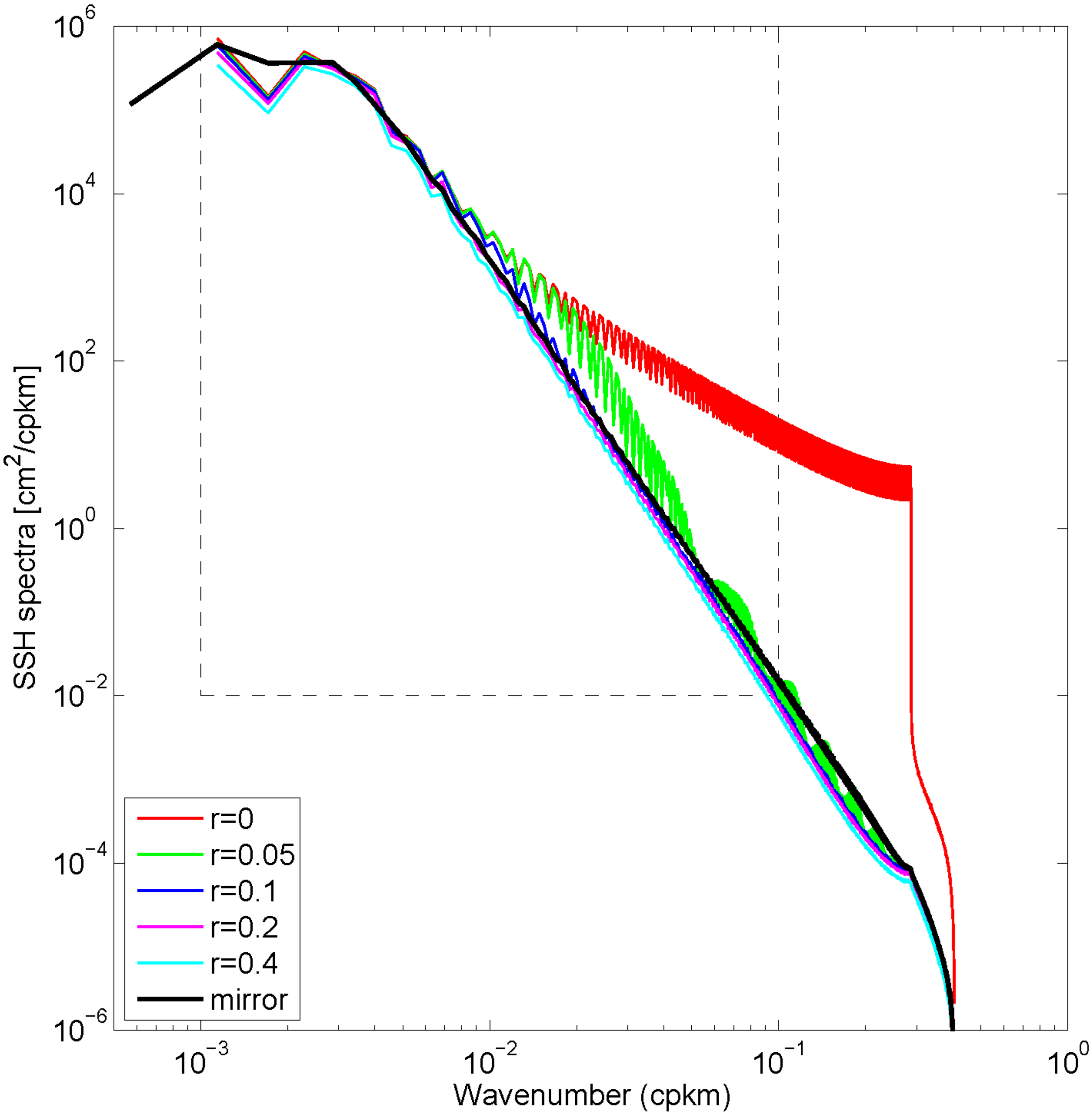

Figure 19. *SSH power spectra computed over the 20°x10° red box in Figure 11 using mirror (black) and tapered cosine windows of different size (none, 5%, 10%, 20% and 40%). Results based on 1-year average (year 20) of the 1/50° simulation.*

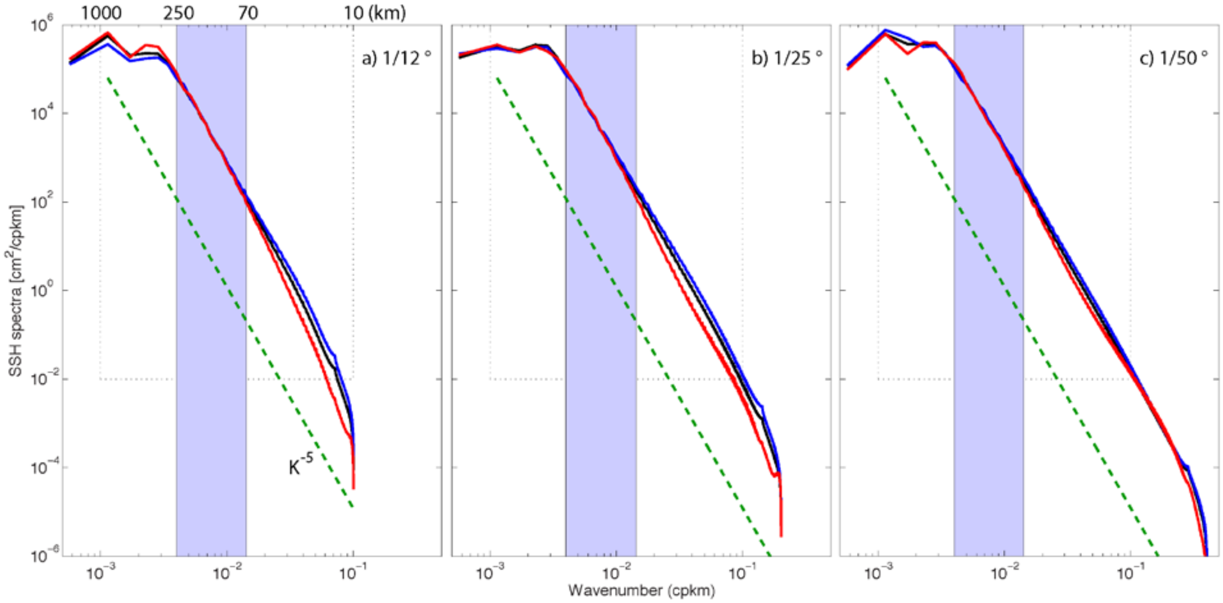

Figure 20. *SSH power spectra in the energetic Gulf Stream region (the 20°x10° box in Figure 11) computed from daily averaged model outputs of year 20 for 1/12°, 1/25°, and 1/50° simulations. The black lines are annual mean; red and blue lines are average over summer and winter, respectively. The green dash line corresponds to k-5 and the shaded area brackets the 70-250 km mesoscale range.*

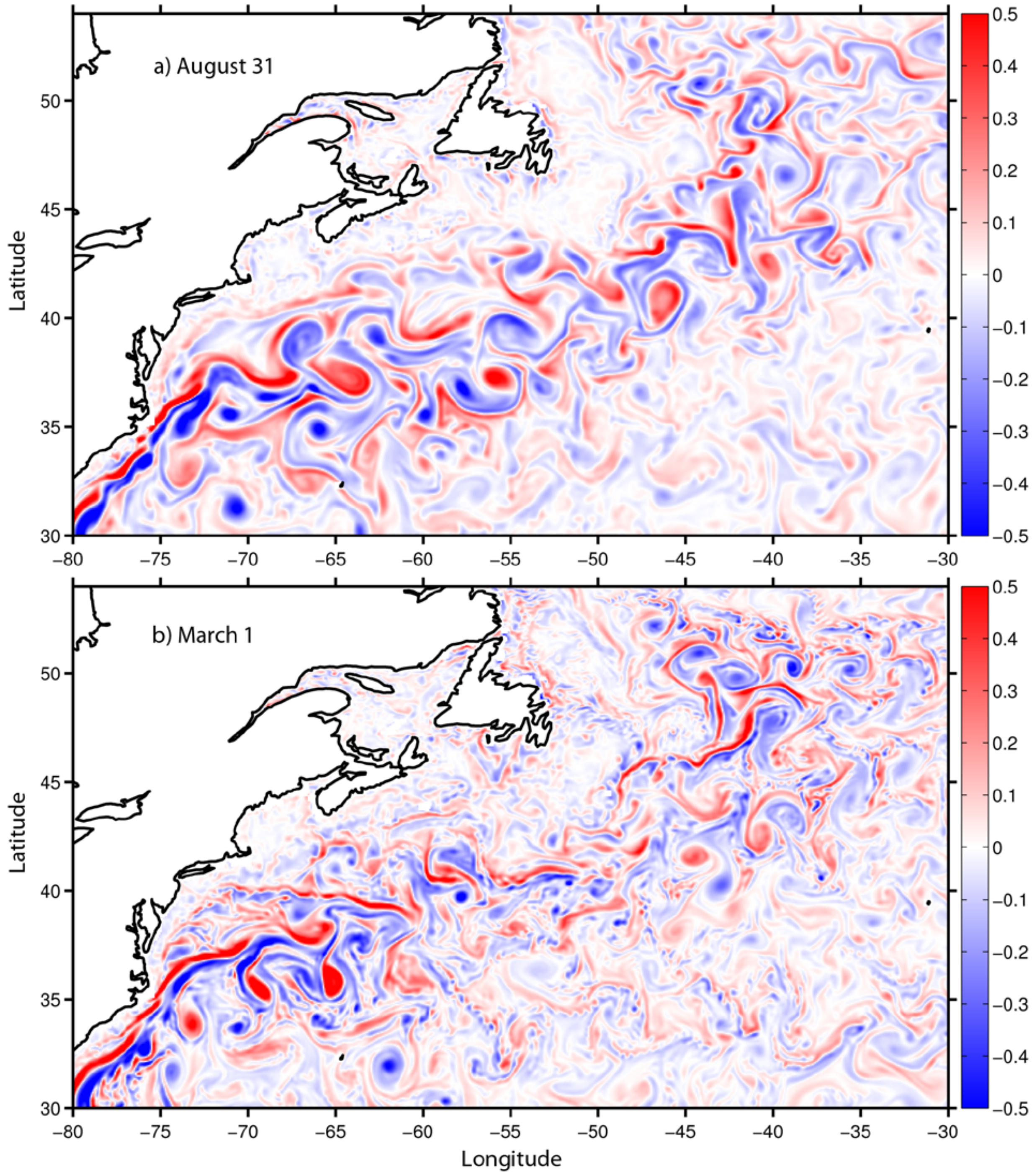

Figure 21. *A snapshot of dimensionless surface relative vorticity (ζ/f with $f=10^{-4}$ s^{-1}) in the Gulf Stream region in summer (August 31) and winter (March 1) of year 20 of the 1/12° simulation.*

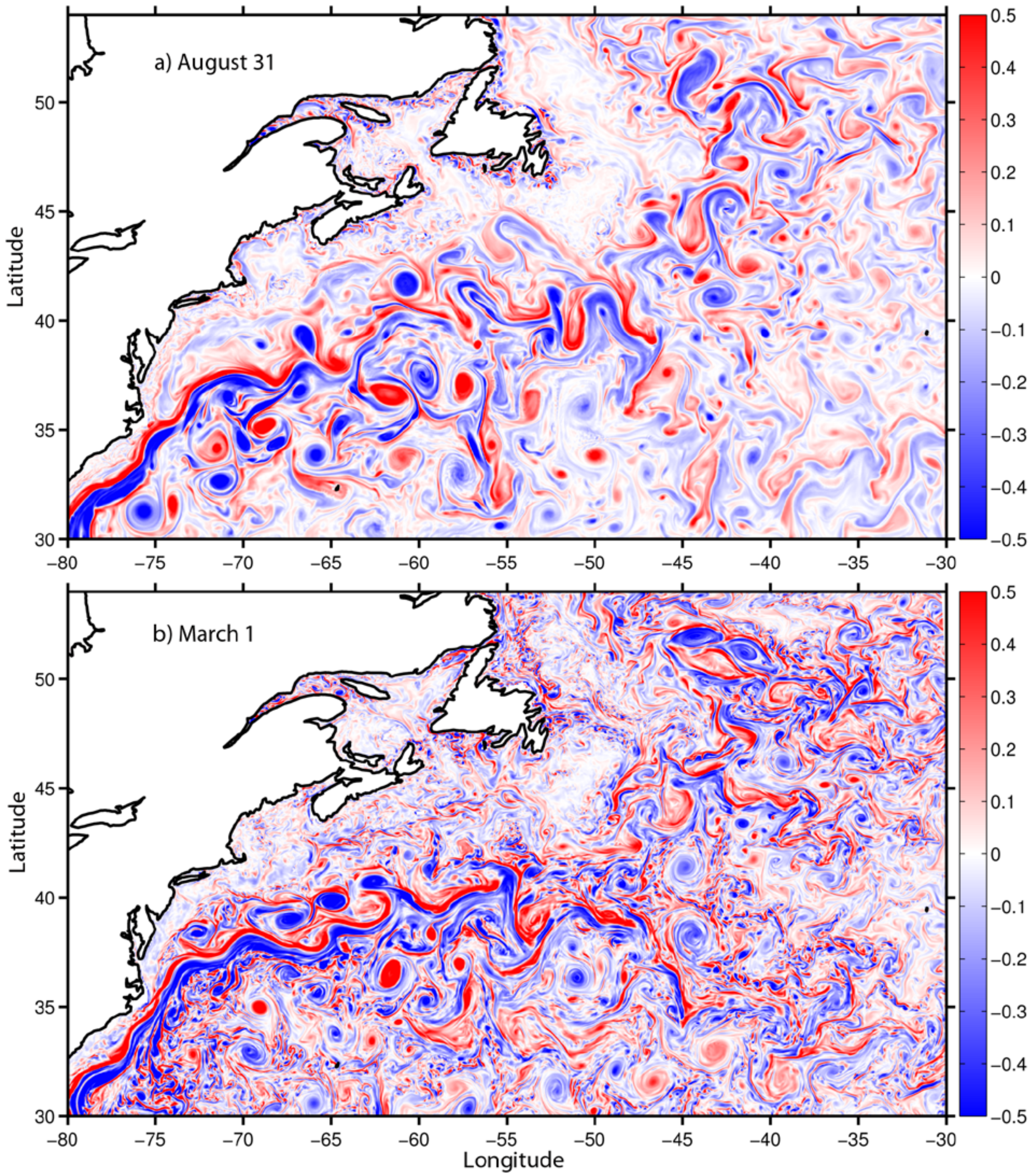

Figure 22. *A snapshot of dimensionless surface relative vorticity (ζ/f with $f=10^{-4}$ s^{-1}) in the Gulf Stream region in summer (August 31) and winter (March 1) of year 20 of the 1/50° simulation.*

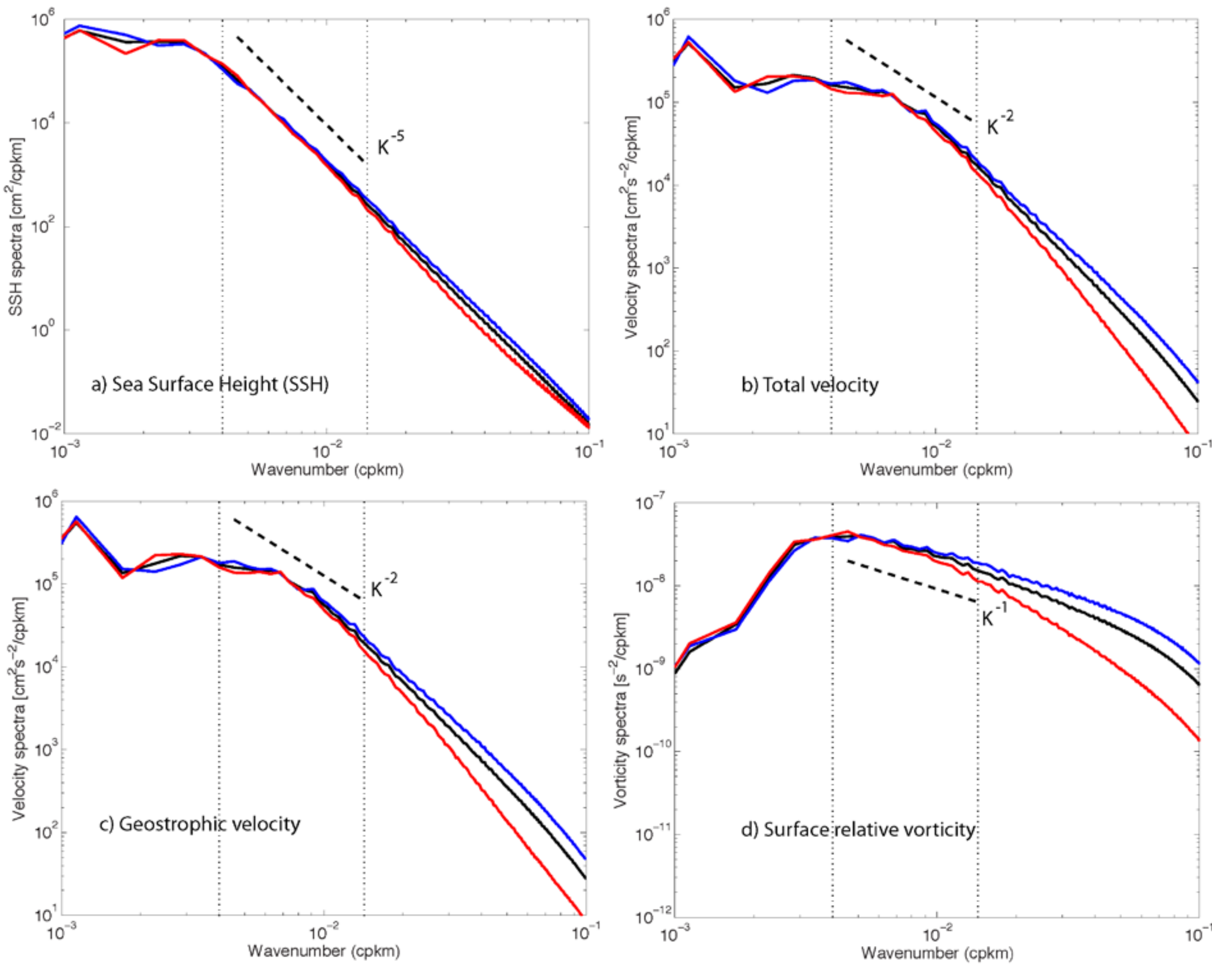

Figure 23. *Power spectra in the energetic Gulf Stream region (red box in Figure 11) computed from daily averaged outputs of year 20 for the 1/50° configuration: a) SSH, b) total surface velocity, c) SSH-derived geostrophic velocity, and d) surface relative vorticity. Annual, summer, and winter mean power spectra are denoted in black, red, and blue, respectively.*

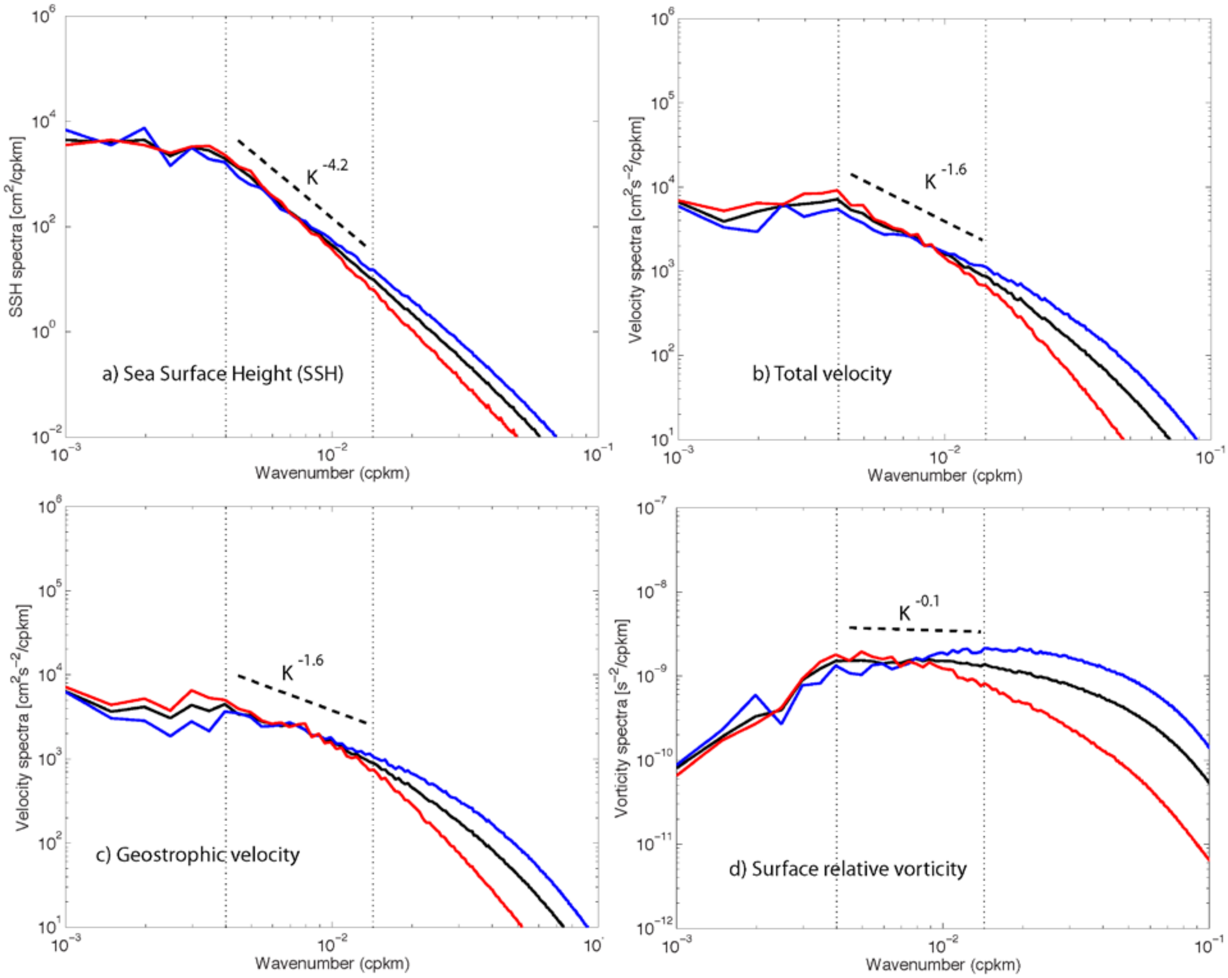

Figure 24. *Power spectra in a less energetic northeast Atlantic region (20-30°N, 20-40°W, see Figure 25) computed from daily averaged outputs of year 20 for the 1/50° configuration: a) SSH, b) total surface velocity, c) SSH-derived geostrophic velocity, and d) surface relative vorticity. Annual, summer, and winter mean power spectra are denoted in black, red, and blue, respectively.*

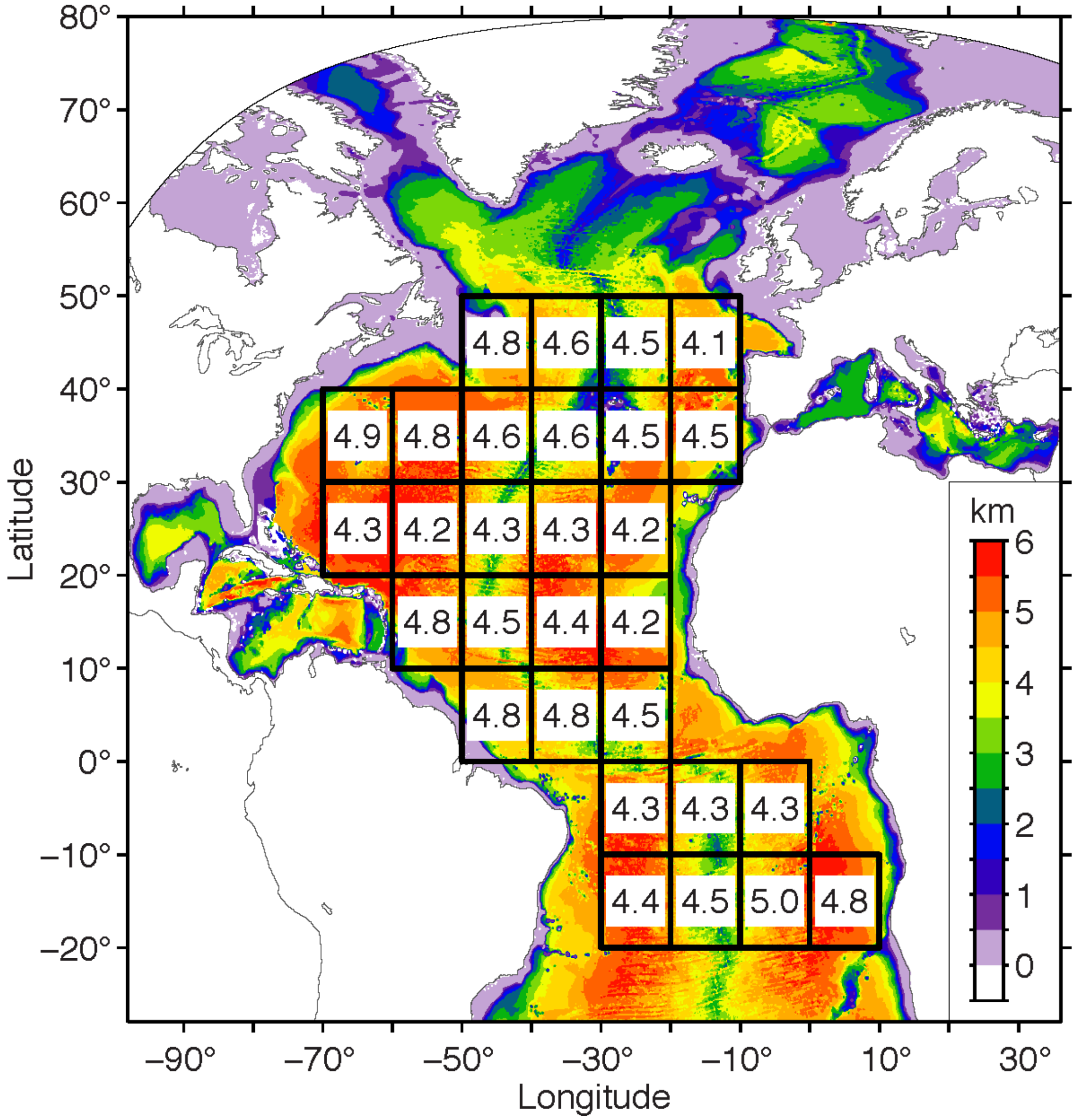

Figure 25. *Sea-surface height power spectra slopes (in the 70-250 km mesoscale range) for 10x10° boxes, calculated from on daily mean outputs for model year 20 of the 1/50° configuration.*

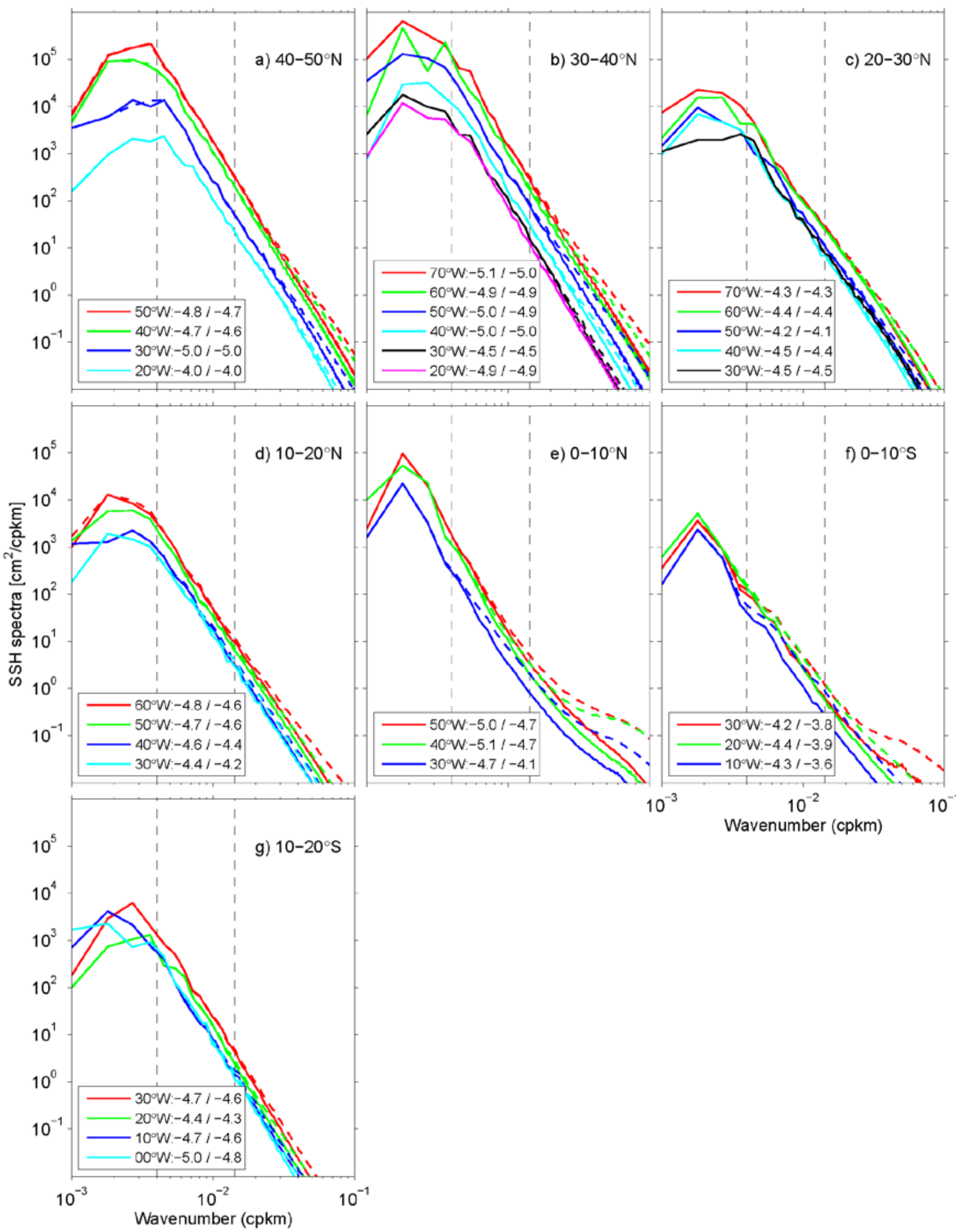

Figure 26. *Sea-surface height power spectra for the 10x10° boxes shown in Figure 25, calculated from daily means (solid lines) and hourly snapshots (dashed lines) for the month of December of year 20 of the 1/50° simulation. The captions in each panel indicate the western-most longitude of the box and the corresponding spectral slopes in the 70-250 mesoscale range (daily and hourly).*